Linear Colliders

J. Alcaraz

CIEMAT, Avda. Complutense, 22, 28040-Madrid, SPAIN, and

CERN, 1211 Genève 23, SWITZERLAND

Abstract

After several years of study, e^+e^- linear colliders in the TeV range have emerged as the major and optimal high-energy physics projects for the post-LHC era. These notes summarize the present status, from the main accelerator and detector features to their physics potential. The LHC is expected to provide first discoveries in the new energy domain, whereas an e^+e^- linear collider in the 500 GeV – 1 TeV will be able to complement it to an unprecedented level of precision in any possible areas: Higgs physics, signals beyond the SM and electroweak measurements. It is evident that the Linear Collider program will constitute a major step in the understanding of the nature of the new physics beyond the Standard Model.

1 Introduction

Most probably, the LEP (Large Electron Positron) collider [1] will be the largest e^+e^- circular collider ever built. At higher collision energies ($\sqrt{s} \gtrsim 300$ GeV) the huge energy losses due to synchrotron radiation make a circular synchrotron unaffordable due to practical limits and cost [2]. From a technological point of view, this fact is enough to justify the research and development in the field of e^+e^- linear colliders in the TeV energy range.

From a scientific point of view, both e^+e^- and hadron colliders are fundamental and complementary machines in the studies at the highest energy frontier. CERN (European Laboratory for Particle Physics) is an example. After a long tradition in hadronic collisions leading to the discovery of the W and Z weak bosons, the e^+e^- LEP machine has been running for more than a decade, and the next project will be the LHC (Large Hadron Collider), a proton-proton collider with $\sqrt{s} = 14$ TeV. In addition, the most sensible option for the post-LHC era [2] is CLIC (Compact Linear Collider) [3], an e^+e^- linear collider working in the $\sqrt{s} \approx 3-5$ TeV range.

These notes summarize the introductory lectures given at the XXIX International Meeting on Fundamental Physics (Sitges, 2001). Most of the presented material is available thanks to the effort of many people who had contributed to the subject. In particular, the TESLA Technical Design Report [4] and the NLC 2001 Snowmass Report [5, 6] are useful guides for those who want to get a detailed, complete and up to date view of the field.

The report is organized as follows. The first sections describe the main accelerator features and international projects. They will be followed by a presentation of some of the proposed detector options, with a special emphasis on the differences with respect to present e^+e^- working detectors. The last sections are devoted to the LC physics potential, and they are mainly based on the material prepared for the European project [7].

2 The Accelerator

2.1 Acceleration in linear colliders

Acceleration cavities are basic units of a linear collider. They are cavities in which stationary electromagnetic waves, in phase with the circulating beam, provide the necessary acceleration up to the required energies. The standard way of providing power to these cavities is via *klystrons*. A klystron (Figure 1) generates high power microwave frequency pulses from the periodic deceleration of an internal electron beam. A low power radiofrequency (RF) cavity (the *buncher* cavity) is responsible for converting the continuous beam into a train of electron bunches. These bunches are then strongly decelerated and the released RF power transferred to an output cavity (the *catcher* cavity).

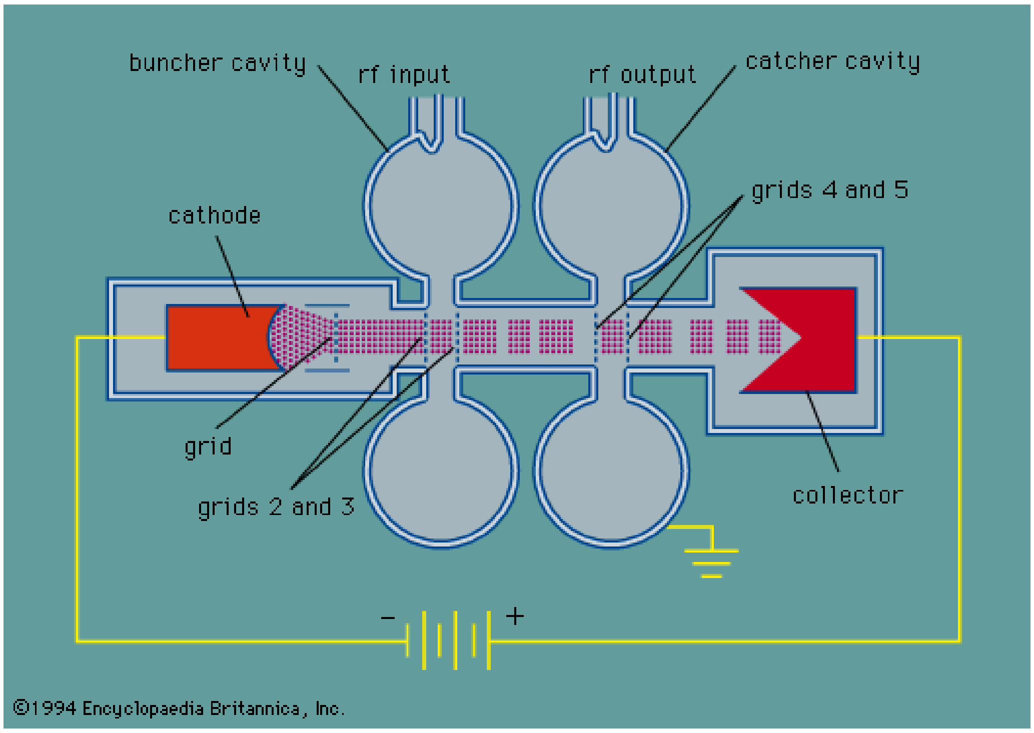

Figure 1: Simplified scheme of a klystron (from the Encyclopedia Britannica).

Presently available klystrons are able to generate pulses with frequencies $\nu \lesssim 10$ GHz. Higher frequencies and cavity gradients, like those of the CLIC project, require alternative acceleration procedures. Figure 2 shows a scheme of the CLIC project. In order to obtain energies as large as $\sqrt{s} \gtrsim 3$ TeV in a reasonable length ($\lesssim 30$ km), gradients above 100 MV/m are necessary. The basic idea is to decelerate bunches of a secondary electron beam of moderate energy ($E \simeq 2$ GeV) to obtain a power source of very high frequency ($\nu \simeq 30$GHz). In a very naive view, the whole idea behind CLIC is to build a huge klystron-like structure. A large part of the secondary beam complex is dedicated to the formation of bunch trains with the adequate structure and frequency for the deceleration step.

The CLIC project involves new concepts requiring large R&D efforts, and it must be considered as a long-term project (> 10 years). Based on the present state-of-the-art, one has to rely on more conventional schemes in order to built a linear collider within a reasonable time scale ($\lesssim 10$ years). The price to pay is a more modest energy reach ($\sqrt{s} = 500$ GeV – 1 TeV). Table 1 shows the different options investigated. Apart from the CLIC concept, all linear accelerator projects use (more or less) conventional acceleration schemes. Note that all microwave bands [1] are considered. A special case is that of the SLC (Stanford Linear Collider). It constitutes a unique source of experience in the field, since it is the highest energy linear accelerator successfully built and operated.

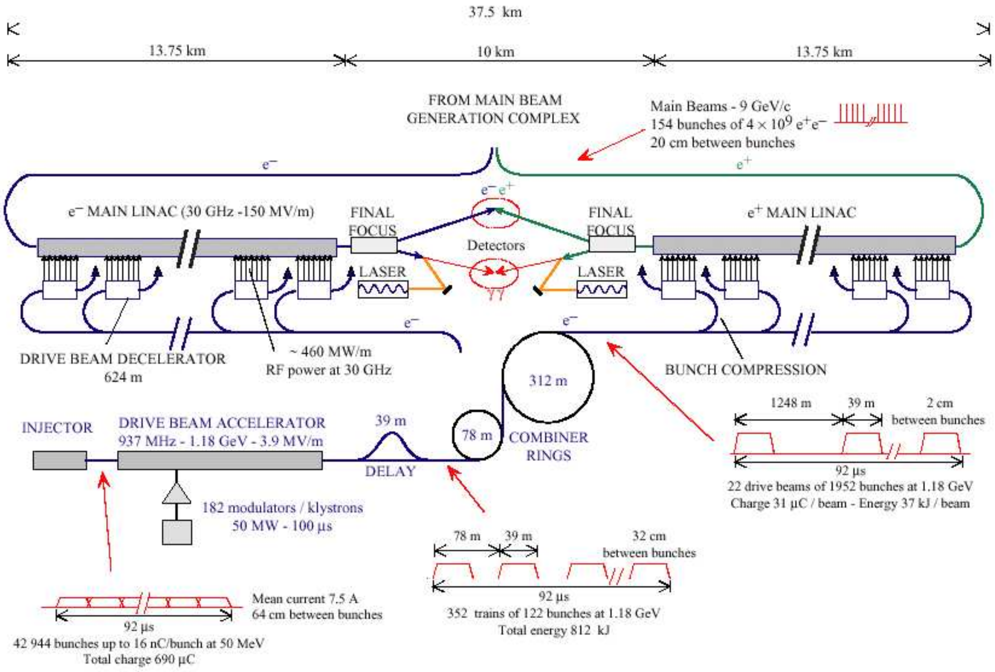

Figure 2: Scheme of the CLIC (Compact Linear Collider) [3].

Three projects are presently under development at the international level:

- The NLC (Next Linear Collider) is the American project [5]. The option chosen for this design maximizes the accelerating gradient by maximizing the frequency of the cavities. The X-band constitutes a new environment in acceleration, with new features and problems to face.
- The Japanese project, JLC (Japanese Linear Collider), is similar to the NLC project in its basic design [8]. An alternative, the C-band option, which may help to solve some of the problems associated to the high-frequency scenario, is also considered.
- Finally, the European project, TESLA (TeV Energy Superconducting Linear Accelerator), adopts a new approach for obtaining higher gradients. Instead of entering a high-frequency domain, a maximal power transfer to the electron beam is obtained by the use of superconducting accelerating cavities and a minimization of power losses. This accelerator would work in the L-band, even below the frequency range of the present SLC collider. The price to pay is medium-term R&D effort in the frontier of superconducting technologies, aiming to obtain stable gradients in the range 25 – 35 MV/m.

2.2 Linear Accelerator features at the TeV

In order to guarantee a reasonable physics potential at TeV energies, high luminosity is a must. Most of the interesting processes present cross sections which decrease with energy as

[1] The notation L band,...,K band has been inherited from the notation used in radars.

Table 1: Present and future e^+e^- linear accelerator projects.

Band	Frequency Range (GHz)	Accelerator Project
L	1-2	TESLA (1.3 GHz)
S	2-4	SLC (2.9 GHz)
C	4-8	JLC C-band (5.7 GHz)
X	8-12	NLC/JLC (11.4 GHz)
K	12-40	CLIC (30 GHz)

$1/s$. In practice, one is talking about luminosities $\mathcal{L} \gtrsim 10^{34}$ cm^{-2} s^{-1}. In terms of accelerator parameters, the relevant formula is given by:

$$\mathcal{L} \;=\; \frac{n\, N^2 \nu}{4\pi\, \sigma_x \sigma_y}\, H_D, \tag{1}$$

where n is the number of bunches per train, N is the number of particles per bunch, ν is the train frequency, and σ_x, σ_y are the transverse spot sizes, assuming collisions along the Z axis. H_D is an additional factor (a disruption coefficient) which will be discussed later. Luminosities above 10^{34} cm^{-2} s^{-1} typically imply: number of bunches per train as large as 4500 (TESLA), train repetition rates as high as 120 Hz (NLC/JLC) and transverse spot sizes as small as few nanometers (TESLA/NLC/JLC).

2.2.1 Beamstrahlung

The transverse beam spot sizes, σ_x and σ_y, should be kept as small as possible in order to maximize the luminosity. However, there is an effect, called beamstrahlung (Figure 3b), which plays a critical role when sizes become too small. It is caused by the interaction between the electromagnetic field of a bunch and the individual electrons from the opposite beam. The bunch field exhibits huge long-range effects as the bunch approaches a point-like structure, leading to fractional energy losses proportional to $\sqrt{s}/(\sigma_x + \sigma_y)^2$.

In order to simultaneously maximize luminosity and minimize beamstrahlung losses, the best choice is to reduce only one of the transverse components of the spot down to the nanometer level, let us say σ_y, while keeping σ_x relatively large, at the level of few hundred nanometers.

Beamstrahlung effects dramatically increase with the collision energy. As an example, Figure 4 illustrates the beam energy distributions expected at the interaction point (IP) region of the CLIC collider for different $\sqrt{s}$ values. For a maximum potential value of E_{CM} = 5 TeV, only 15% of the total luminosity can be assumed to correspond to collision energies above $99\%\sqrt{s}$. Beamstrahlung makes life difficult since, contrary to the usual case at lower energy e^+e^- colliders (LEP,SLC), and similarly to hadron colliders, the total energy and the total longitudinal momentum of the collision become unknown. Even worse. In order to perform precision physics, not only the luminosity, but also the beamstrahlung distribution functions need be measured accurately [2].

2.2.2 Backgrounds

Beamstrahlung energy losses lead to potentially dangerous backgrounds at the IP regions. Typical examples are photons and e^+e^- pairs, either from the beams or from subsequent interactions with the material. The event shown in Figure 5 illustrates the effect. A large part of these

[2] In this respect, one could try to study some observables under control from the theoretical point of view, like the acollinearity distribution of Bhabha events at low polar angles.

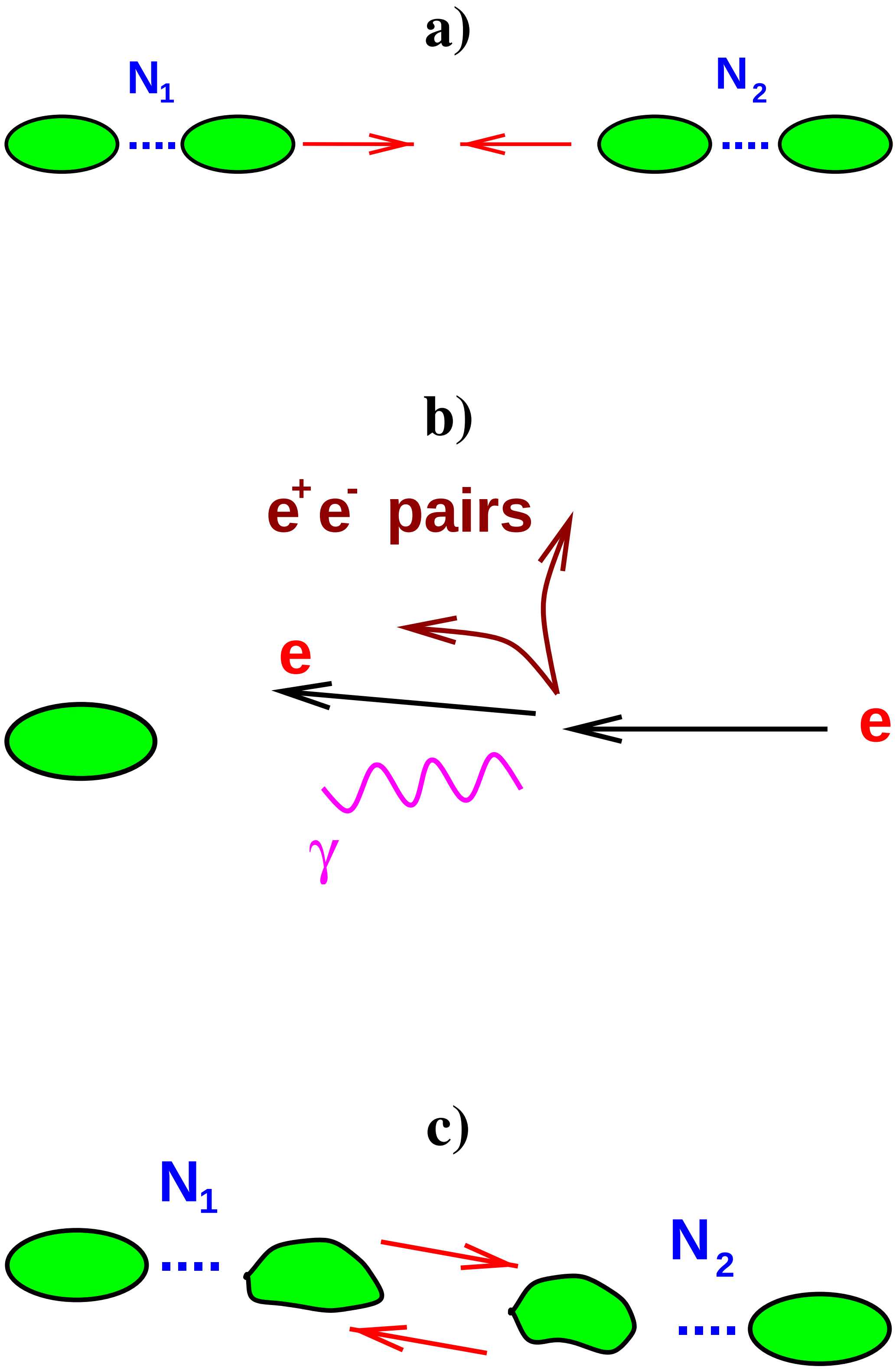

Figure 3: Important effects in TeV e^+e^- collisions at linear colliders: a) ideal situation, b) beam-electron interactions (beamstrahlung), c) beam-beam effects (disruption).

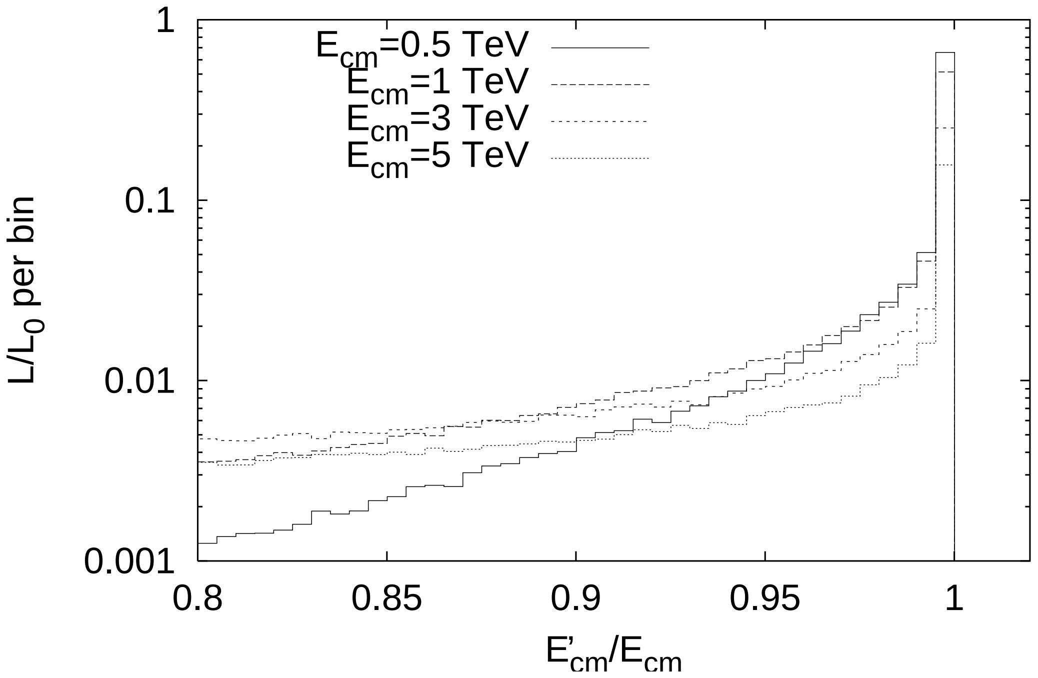

Figure 4: Beamstrahlung effects at high e^+e^- collision energies (CLIC collider [9]). The distributions of the normalized collision energy at the interaction point, E'_{cm}/E_{cm}, are shown for different values of the initial center-of-mass energy E_{cm}. In the absence of beamstrahlung effects: $E'_{cm} = E_{cm}$.

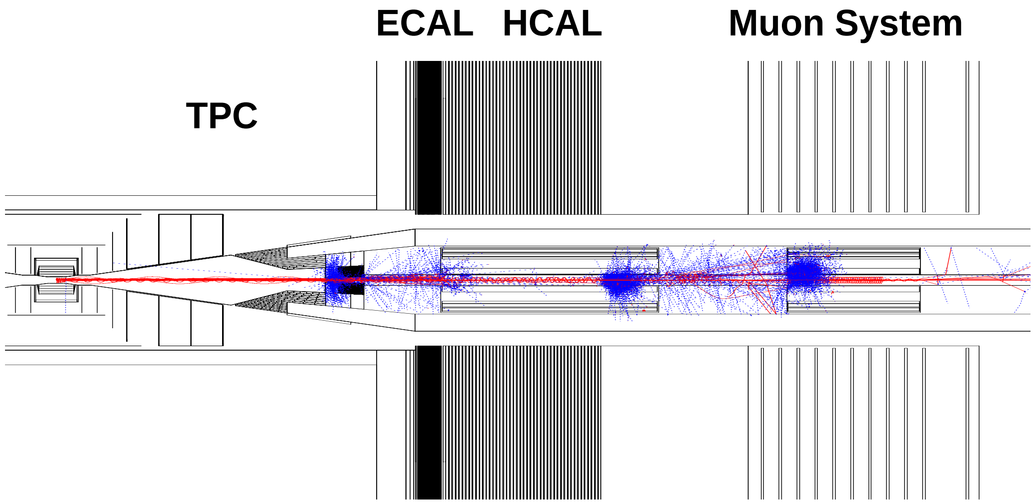

Figure 5: Visual representation of background effects close to the interaction region for a TESLA event [10]. The huge background at low angles forces the use of masks.

backgrounds are eliminated by the use of masks at very low polar angles ($\theta \lesssim 80$ mrad), also shown in the figure. Backgrounds remain a delicate issue even after the use of masks. Figure 6 shows the occupancy at different layers of a typical microvertex detector (TESLA). In order to protect the pattern recognition procedures against huge combinatorial backgrounds, pixel-like detectors (with intrinsic 3-dimensional information) must be employed.

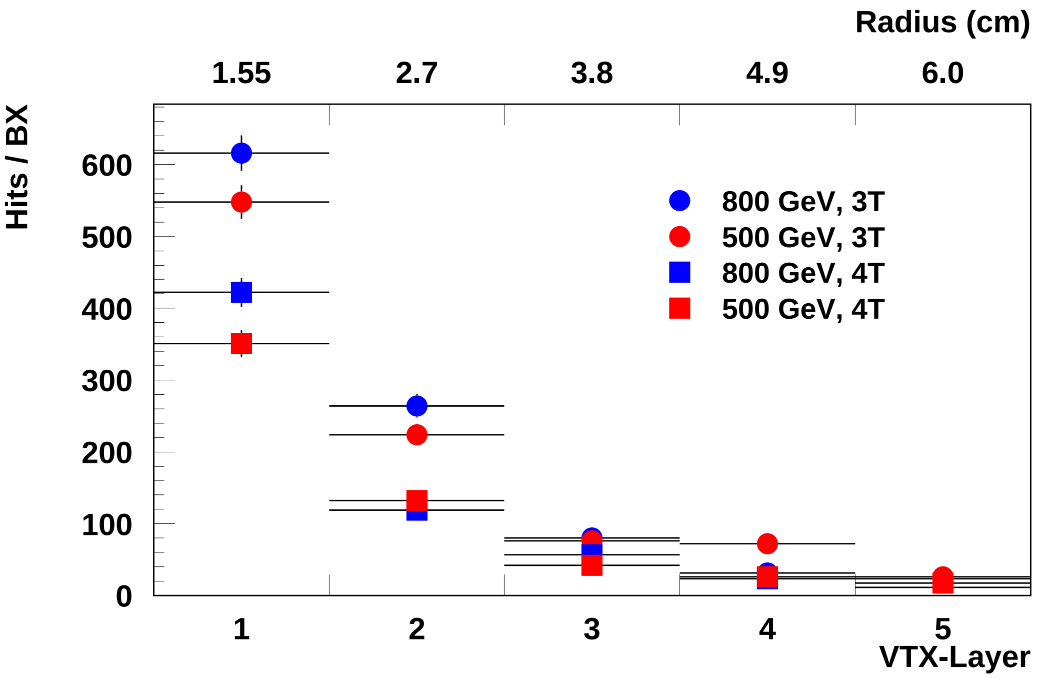

Figure 6: Occupancy at the various layers of a microvertex detector proposed for TESLA [10]. Lower values of the layer number correspond to smaller distances with respect to the interaction point. Values are shown for different choices of the center-of-mass energy and of the solenoidal magnetic field. Higher energies lead to an increase of the background flux. Larger magnetic fields trap charged particles in trajectories at lower radii, thus reducing it.

2.2.3 Beam-beam effects

Finally, we briefly discuss beam-beam related effects (Figure 3c). Given their small size, bunches of different beams are able to feel each other before collision. As a consequence the bunch shapes get modified, in the phenomenon known as *disruption*. Sizes are also affected by the *pinch effect*: in the e^+e^- case the attraction between bunches of opposite charge leads to smaller crossing sections and therefore to higher luminosities. The H_d factor in Formula 1 accounts for this enhancement (typical numbers for H_d are in the range $1.5-2$). All these effects are difficult to control a priori, and correction/monitoring systems are envisaged in all accelerator designs.

2.3 A closer look to the different accelerator projects

Table 2 shows the main design parameters of the NLS/JLC, TESLA and CLIC proposals. Let us comment on some specific features:

- A scheme of the NLC accelerator complex is shown in Figure 7. Effective gradients close to 50 MV/m are envisaged. The high RF-frequency (X-band) leads to a small separation between bunches (1.4 ns) and forces a design in which the beam collisions occur with a certain angle, in order to avoid disruption effects from the multiple bunch crossings.

- A scheme of the structure proposed for TESLA is presented in Figure 8. Although the accelerating gradient (25 MV/m) is smaller than in the NLC/JLC case, the use of superconducting cavities and the minimization of power losses lead to similar acceleration capabilities. An advantage of the TESLA approach is that it works in the L-band. Low RF frequencies imply a suppression of wakefield effects (electromagnetic fields associated to the accelerated beam which act back on the next beam), thus making the task of keeping small emittance easy. The large separation between bunches (337 ns) permits the installation of a feedback system [11] acting before the next bunch crossing. Head-on collisions are possible in this case, since a bunch can be deflected before the next bunch of the opposite beam comes in (as shown in the accelerator design of Figure 8).
- Some of the main features of the CLIC project (Figure 2) have been discussed in previous sections. All typical features and problems associated to high RF-frequency become more pronounced in this case (wakefields, separation between bunches (0.67 ns), beamstrahlung effects, feedback systems, …).

Table 2: Design parameters of NLC/JLC, TESLA and CLIC e^+e^- collider projects. Numbers are shown for a first stage at $\sqrt{s} = 500$ GeV.

	NLC/JLC	TESLA	CLIC
Luminosity (10^{34} cm^{-2} s^{-1})	2.0	3.0	1.4
RF Band	X	L	K
Acceleration gradient (MV/m)	50	25	150
Repetition Rate, ν (Hz)	120	5	200
Bunches/Pulse, N_1, N_2	190	2820	154
Bunch separation (ns)	1.4	337	0.7
Bunch transverse size, σ_x (nm)	245	553	202
Bunch transverse size, σ_y (nm)	2.7	5	2.5
Bunch length, σ_z (μm)	110	300	30
Beamstrahlung Momentum Spread (%)	4.7	3.3	4.4
Pinch Enhancement, H_D	1.4	≈ 2	1.8
Transverse emittance, $\gamma\varepsilon_x$ (10^{-8} rad m)	360	1000	200
Transverse emittance, $\gamma\varepsilon_y$ (10^{-8} rad m)	3.5	3	2

2.4 Versatility

One of the most interesting features of high energy e^+e^- linear colliders is their versatility. First of all, they are conceived as evolving facilities. They can start at moderate energies ($\sqrt{s} \simeq 500$ GeV) and increase their collision energy in successive stages, according to time and budget constraints. At any time, and given their high luminosity capabilities, they can provide dedicated runs at lower energies in order to do high precision measurements (m_t, m_W, electroweak observables at the Z-pole, …).

Concerning beam versatility, another interesting feature -which we will not discuss from the technical point of view- is the ability of providing collisions with polarized beams. Typical longitudinal polarizations of $\mathcal{P}_{e^-} = 0.8$ and $\mathcal{P}_{e^+} = 0.6$ for the e^- and e^+ beams, respectively, are considered in the analyses of the next sections.

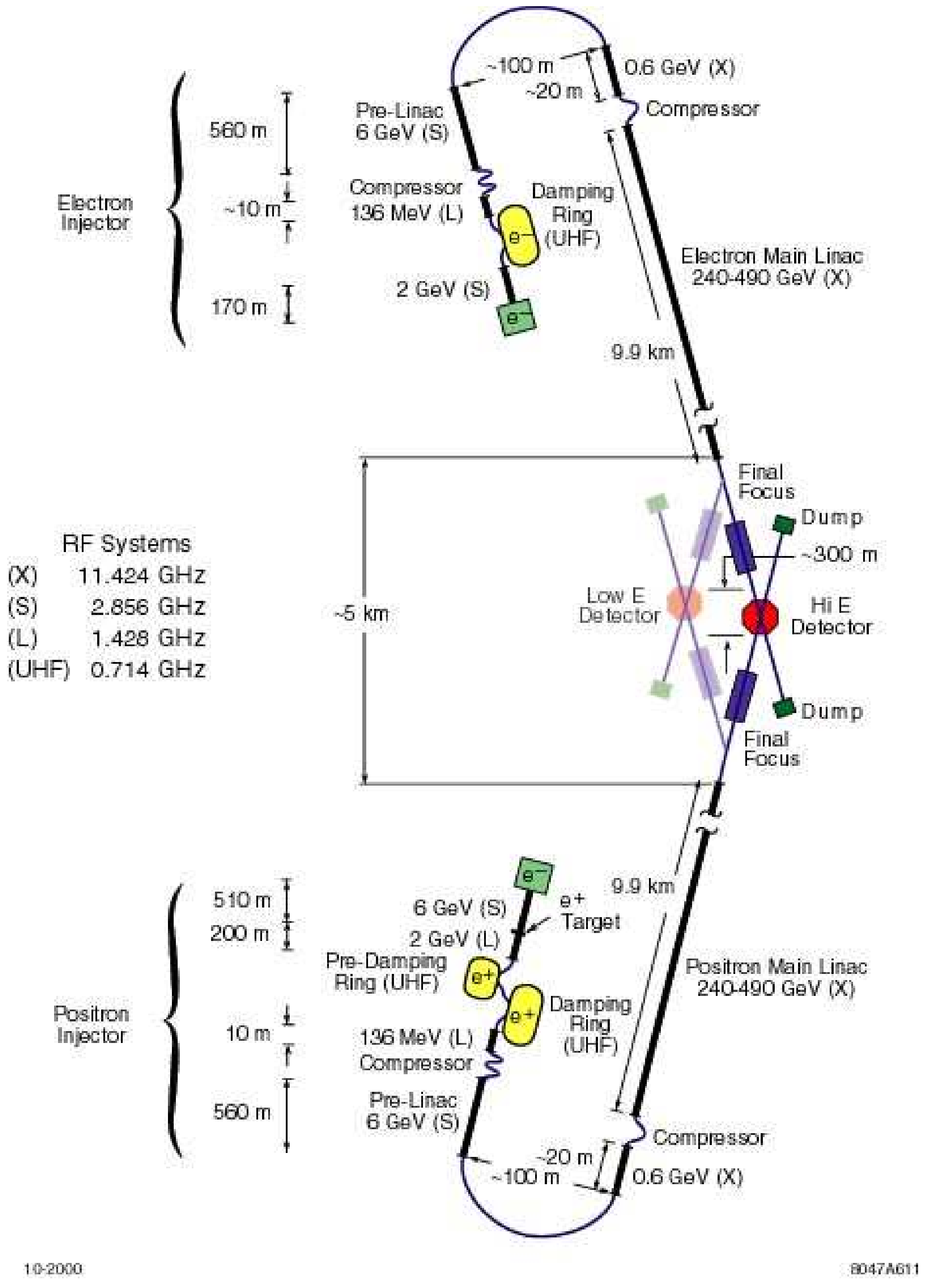

Figure 7: Scheme of the NLC [5].

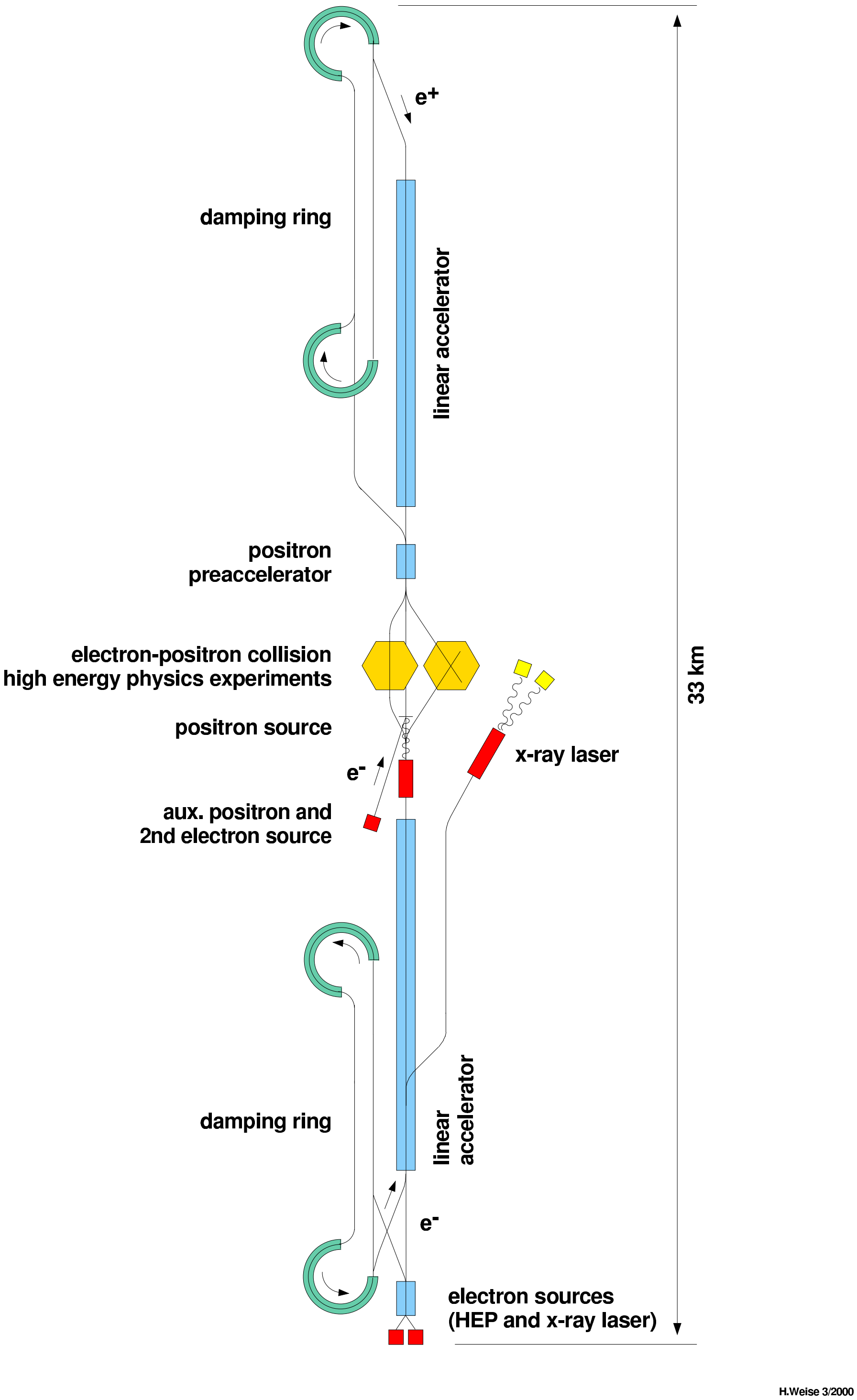

Figure 8: Scheme of the TESLA collider [11].

Not only e^+e^- collisions are possible, but also e^-e^-, $e\gamma$ and $\gamma\gamma$. A γ beam may be obtained by Compton back-scattering of an electron beam and a laser beam. Photon energies up to 80% of the total electron energy are obtained, with reasonable luminosities ($\mathcal{L}_{\gamma\gamma} \sim 0.2\ \mathcal{L}_{e^+e^-}$). Although we will not discuss them in detail, one should keep in mind that any of these options may become interesting in due time, depending on the nature of the physics found at the TeV scale [12].

Last but not least, there exist interesting physics applications outside Particle Physics, an obvious example being the case of TESLA, where a SASE (Self Amplified Spontaneous Emission) FEL (Free Electron Laser) facility is envisaged [13], with an enormous range of application (Solid State Physics, Biology, Medicine, …).

3 The Detector

In principle, a detector for a future e^+e^- linear collider should not differ much from those presently used at the Z pole. Figure 9 shows the proposed detector designs for the JLC and TESLA options. From a qualitative point of view, the different subdetectors are disposed in a standard way, from the IP to the outermost radius: microvertex, central tracker, electromagnetic calorimeter, hadronic calorimeter, solenoidal magnetic field and muon detector. However, advances in detector technology, many of them driven by the LHC program, suggest the construction of more perfomant detection systems. TeV collision energies imply a detector with the following capabilities:

- Maximal coverage and hermeticity, a general requirement for accurate measurements of visible and missing energies.
- High precision tracking, since the relative resolution of tracking detectors degrades proportionally to the momentum ($\Delta p/p \propto p$). The energy requirements for calorimetry are milder, since the relative precision increases with the energy.
- Good track separation and high granularity, due to the high boosts. As an illustrative example, we show in Figure 10 the comparison between a simulated typical $e^+e^- \to W^+W^- \to q\bar{q}q'\bar{q}'$ event at the CLIC collider and a real event at LEP. It is extremely difficult to distinguish the four jets in the CLIC event without good particle separation capabilities.

Based on the acquired experience at the Z pole, important improvements are expected:

- Energy flow reconstruction methods will help to improve the resolution in hadronic environments. Thanks to the high granularity, clusters almost correspond to individual particles. Tracking and calorimetric information can be combined, and many of the particles identified, leading to a sizeable improvement in the reconstruction of the jet energies. Figure 11a shows the expected performance for the TESLA detector design. The mass resolution of the visible mass in Z decays is twice better than that typically obtained with LEP detectors.
- Thanks to the energy flow methods, to the enormous advances in decay length tagging techniques (SLD, LEP) and to new developments in microvertex detectors, one expects to be able to perform b-quark, c-quark and tau identification with high purities and efficiencies. This opens up a new era in precision physics, with all particles classified almost on an event by event basis (electrons, muons, photons, τ, b, c and light quarks). An illustrative plot is that of Figure 11b. Extremely pure samples of b and c quarks can be selected with efficiencies of 60% and 40%, respectively, much beyond the best present detector performances (SLD).

Table 3 provides more detailed information about the performances expected at TESLA.

a)

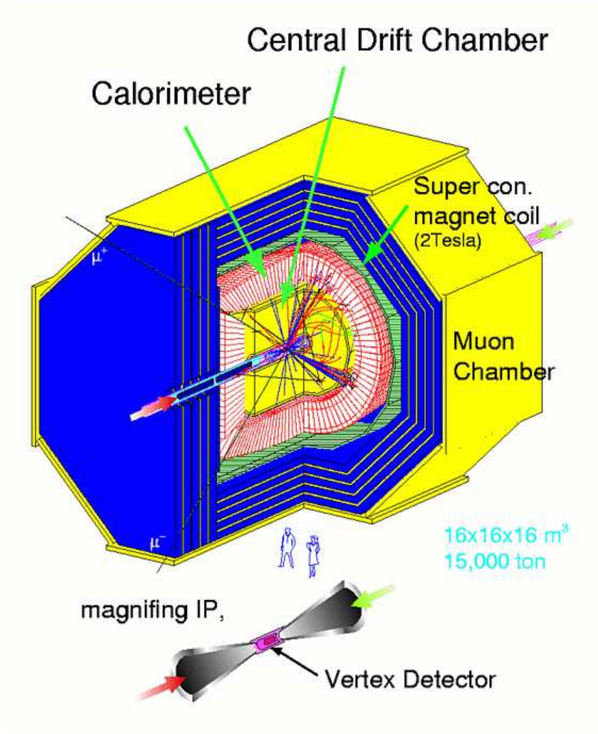

b)

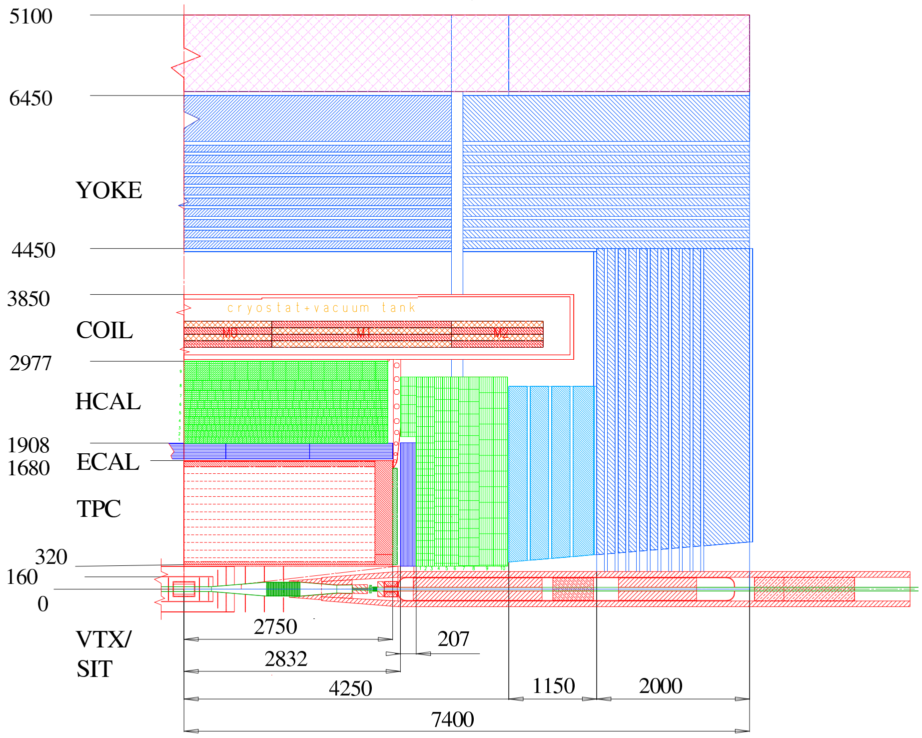

Figure 9: Scheme of typical detectors proposed for the a) JLC and b) TESLA linear colliders.

a)

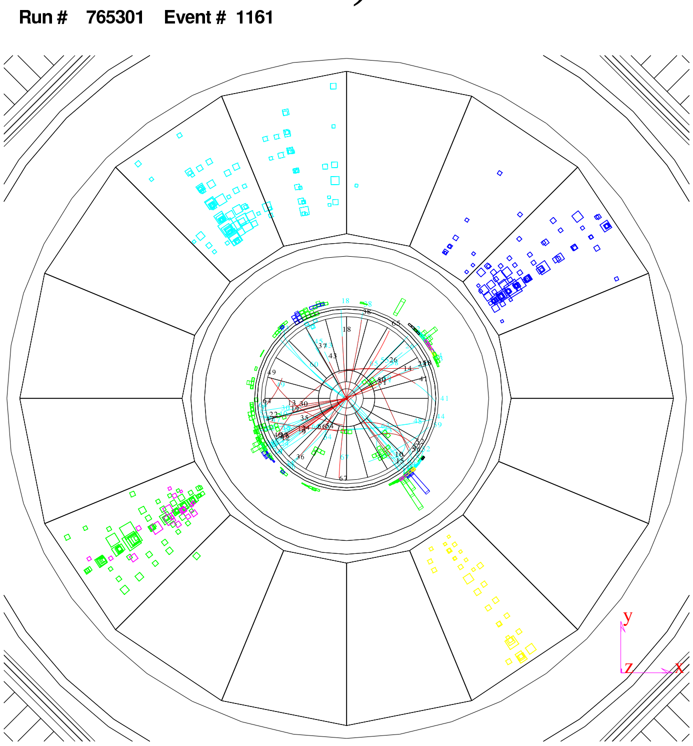

b)

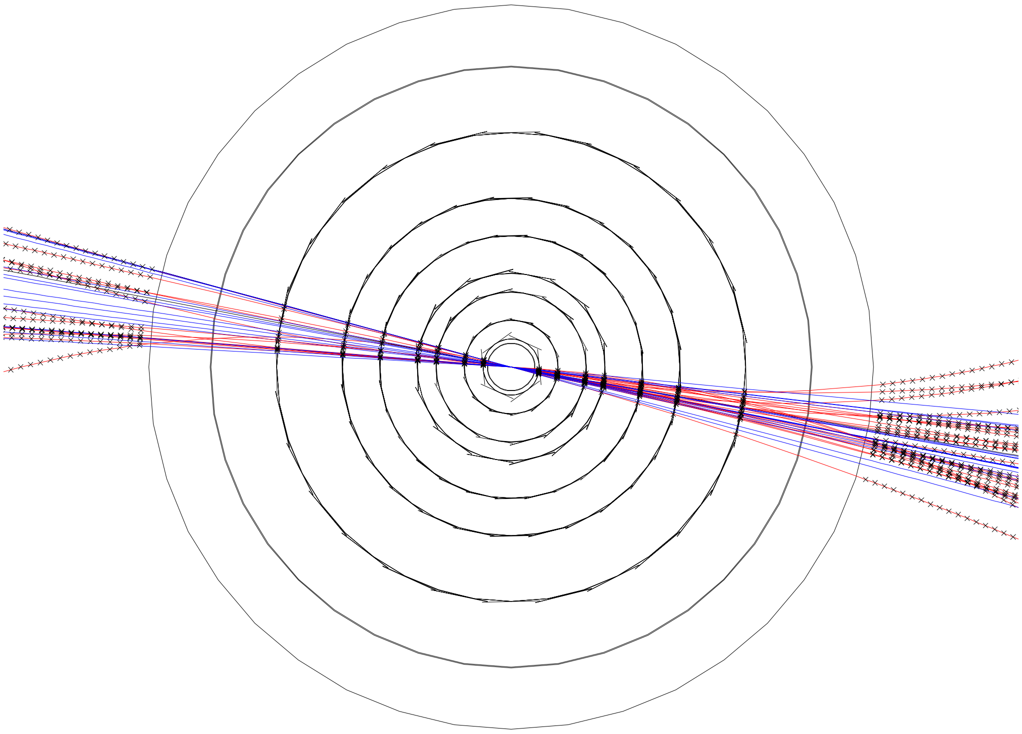

Figure 10: An $e^+e^- \rightarrow W^+W^- \rightarrow q\bar{q}q'\bar{q}'$ event as seen by: a) LEP (real data from the L3 detector at $\sqrt{s}$ = 200 GeV), and b) CLIC (simulated at $\sqrt{s}$ = 3 TeV [9]). The huge boosts at TeV energies change the event topology in a drastic way. Good track separation and high granularity become thus mandatory.

Table 3: Goals of the proposed TESLA detector [10].

Subdetector	Goal
COIL	4 T, uniformity $\leq 10^{-3}$
Vertex Detector (VTX)	$\delta(IP_{r\phi,z}) \leq 5 \oplus \frac{10}{p\ \sin^{3/2}\theta}$ μm (p in GeV/c)
Central Tracker (TPC)	$\delta(1/p_t)_{TPC} < 2\ 10^{-4}(\ \mathrm{GeV}/c)^{-1}$
	$\sigma(dE/dx) \leq 5\%$
Electromagnetic Calorimeter (ECAL)	$\frac{\delta E}{E} \leq \frac{10\%}{\sqrt{E}} \oplus 1\%$ (E in GeV)
	Fine granularity in 3D
Hadronic Calorimeter (HCAL)	$\frac{\delta E}{E} \leq \frac{50\%}{\sqrt{E}} \oplus 4\%$ (E in GeV)
	Fine granularity in 3D
Fe Yoke (MUON)	Tail catcher and efficient muon tracker
Tracking Overall	$\delta(1/p_t) \leq 5\ 10^{-5}(\ \mathrm{GeV}/c)^{-1}$
	$\leq 10\ \mu$m
Energy Flow	$\frac{\delta E}{E} \approx \frac{30\%}{\sqrt{E}}$ (E in GeV)

3.1 Large or small detector? S design

The TESLA option assumes the construction of a detector with a large central tracking gas chamber (most probably a TPC), similar to the designs that have been operated with success at LEP/SLD detectors. The advantage of this configuration is that it offers in a natural way high precision tracking (long lever arm), particle identification (via dE/dX) and high granularity (large radius at the calorimeters).

The American project is also considering the option of a smaller detector (*S* design). Advances in solid-state tracking technologies in the last years have been so important that one could realistically think of a small radius (< 1 m), very precise central tracking detector, as a viable option (Figure 12). There are minor differences with respect to a large detector option (*L* design) in what concerns resolution (Figure 13), but the physics potential of both choices is similar. A compact detector offers a slightly better potential for accurate impact parameter measurements, while a large detector (many measured points, long level arm) guarantees an optimal momentum resolution. Advantages of the *S* option are: a) possibility of using higher magnetic fields in smaller volumes, b) reasonable cost (less calorimetric volume) with an excellent tracking performance. Disadvantages are: a) more sophisticated calorimetry in order to get high granularities, b) complicated pattern recognition (particles are closer to each other near the interaction point), c) higher sensitivity to inefficiencies and noise occupancy (only few points along the trajectory are measured).

3.2 Microvertex detector options

One of the fields where more advances are expected is microvertexing. Contrary to the case of e^+e^- colliders at lower energies, higher backgrounds are expected. They mainly affect the regions close to the interaction point and at lower angles with respect to the beam. We have shown in a previous section how does this affect the occupancy at the first layers of the microvertex detector (Figure 6). This feature imposes the use of pixel-like silicon detectors, in order to suppress combinatorial backgrounds. Point resolutions below 10 μm are a must.

An interesting is a CCD (Charged Coupling Device) based detector, an option already used with success by the SLD Collaboration. Even if it is a well known technology, there are still some issues requiring a dedicated R& D program: a) their dead-time is too long for high collision

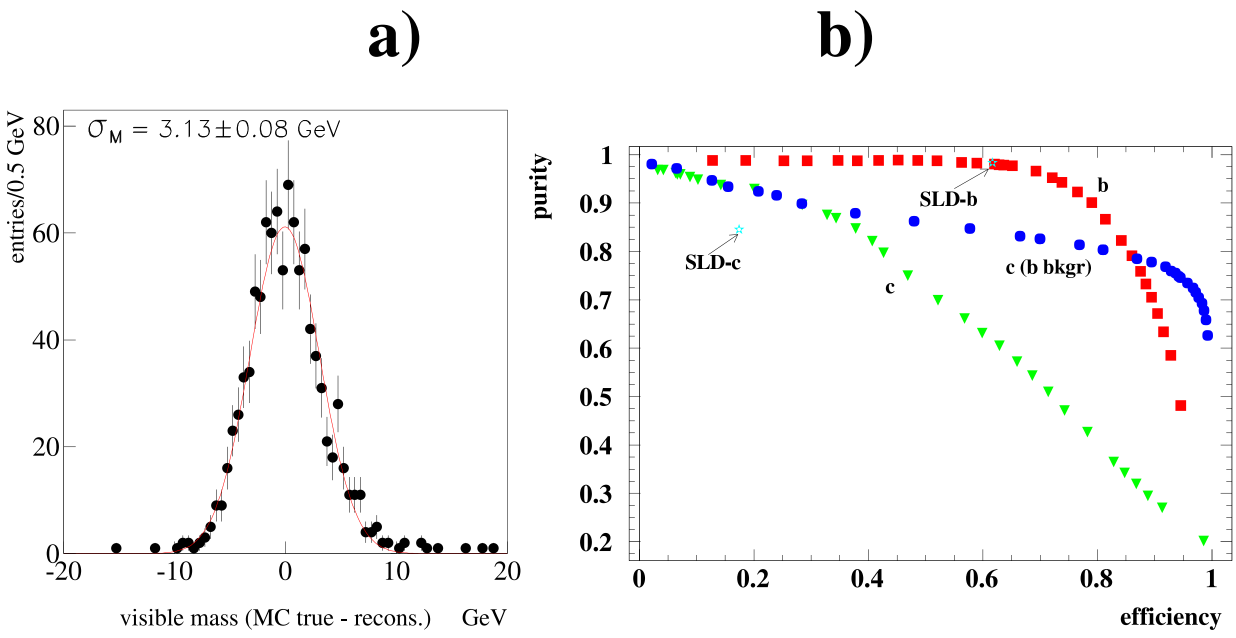

Figure 11: Special reconstruction features at an e^+e^- high energy linear collider. The plots correspond to the TESLA detector design [10]. In Figure a) the invariant mass resolution in Z decays is shown. The obtained width is twice narrower than the those of LEP detectors. In Figure b) the purity versus efficiency plots for the selection of heavy quarks at TESLA are compared to those of the best running e^+e^- detector (SLD). The points identified as c (b background) are the c-quark points measured on a sample without light quarks, thus showing the performance in a sample closer to the environment expected in Higgs decays.

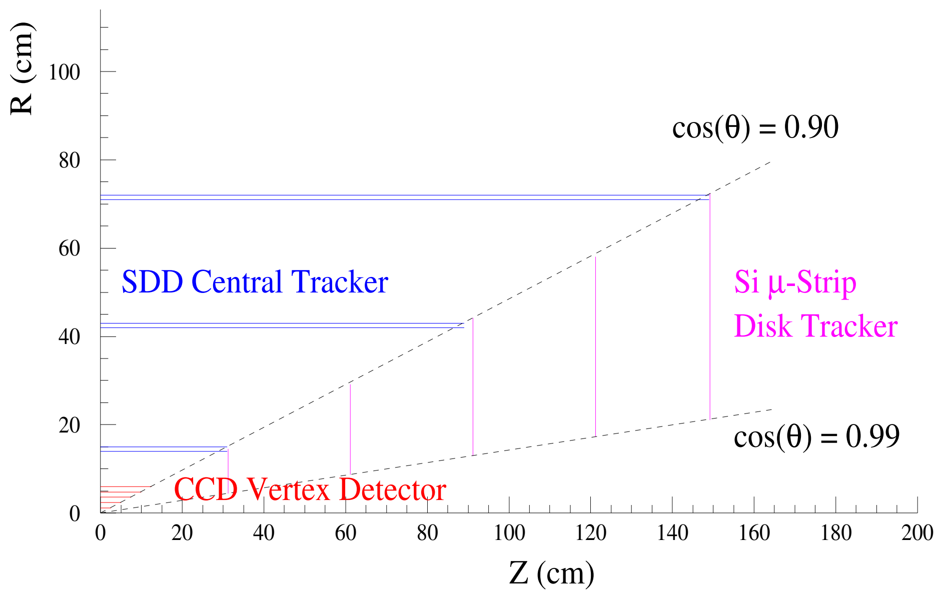

Figure 12: Small detector option for the NLC.

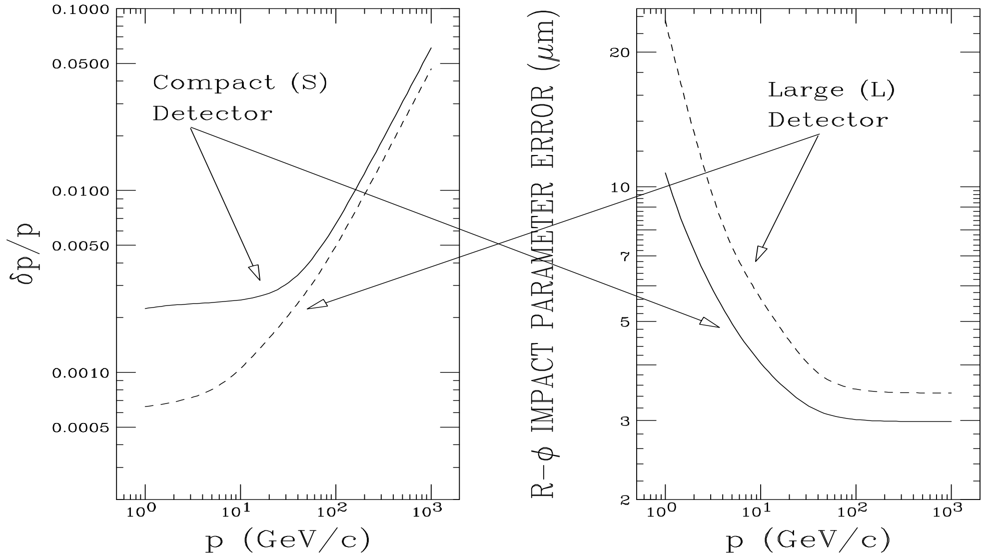

Figure 13: Comparison between the performances of large and small detector design options at the NLC [6].

rates (pixels are read out serially) and b) they are potentially sensitive to radiation backgrounds. Problem a) might be solved by a parallel readout of the CCD columns (Figure 14). Problem b) -if it turns out to be critical- would require an inter-disciplinary effort.

These problems do not exist in the case of HPS (Hybrid Pixel Sensors). They offer individual readout for each pixel and better radiation hardness properties. The R& D work for these options concerns the reduction of the cell size to smaller dimensions (below 50×300 μm^2 size) and the scaling to larger structures. The required resolutions can be obtained even with a partial readout; Figure 14 shows a possible hybrid pixel scheme, with a physical pixel dimension of 50×50 μm^2 read out every 200 μm.

3.3 Central tracking

Here we will only discuss the large detector case, and in particular the TPC (Time Projection Chamber) option. A large experience has been accumulated at LEP, providing confidence that this is the right choice in the framework of the TESLA proposal. Nevertheless, and compared to present environments, a TPC in an e^+e^- linear collider will face new problems:

- Higher backgrounds. Neutrons can be suppressed by an appropriate reduction of hydrocarbons in the gas mixture. The rate of positive ions from primary ionizations is not expected to be so large as to create problems in operation.
- High collision rates. New gating mechanisms in order to stop positive ions (produced during the avalanche) coming back into the drift volume could be necessary. For this purpose, a passive system is advisable, since there is no much time to switch on and off voltages in between collisions.

An attractive way of solving the gating problem (but not the only one) is the installation of GEMs (Gas Electron Multipliers), which are currently in use at several experiments (HERA-B, COMPASS). A GEM [14] consists of a two metallic surfaces separated by a thin polymer layer. It is perforated by a high density of holes, separated from each other by distances of the order of

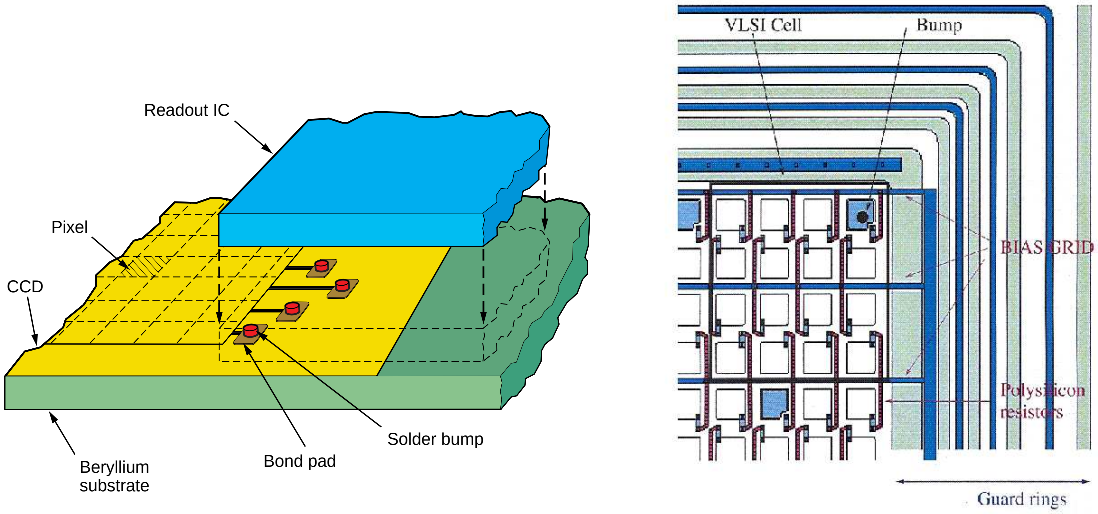

Figure 14: CCD (left) and APS (right) options for TESLA [10]. The first figure shows the parallel scheme for the CCD column readout. The second figure shows a possible hybrid scheme in which only a subsample of all sensors is readout.

100 μm. With this configuration, a huge electric field between the two conducting surfaces can be established, and electron clouds are focused and amplified through the holes in an efficient way (Figure 15). GEMs may solve the problem of back-drifting positive ions, provide a more uniform charge collection and lead to better track separation capabilities. A remaining problem is how to get an optimal position resolution (the electron avalanches have sizes of order 100 μm) by an intelligent geometrical design of the readout pads (they have sizes of the order of mm).

3.4 Calorimetry

The requirements on calorimetry are not too different from those of LEP/SLC: hermeticity, granularity and good energy resolution for jets. The TESLA proposal [10] considers two options for the electromagnetic calorimeter: a shashlik calorimeter (easy assembly, good performance and low cost), and a more pretentious, high-granularity detector, based on Si-W detection slabs (Figure 16).

Concerning hadron calorimetry, the basic option for TESLA is a tile calorimeter using stainless steel or brass as absorber and scintillator plates as active medium. A second possibility is based on the fact that, if the granularity is high, counting hits turns out to be competitive with measuring deposited energies. The feasibility of this “digital” hadronic calorimeter option is illustrated in Figure 16.

3.5 Luminosity measurement and mask

The luminosity detector region must take into account the huge backgrounds expected at low angles. The necessity of masks has already been addressed in previous sections. Figure 17 shows the detailed view of the mask layout for TESLA.

3.6 Trigger and Data Acquisition

The main news concerning the trigger system in the case of the TESLA proposal are that

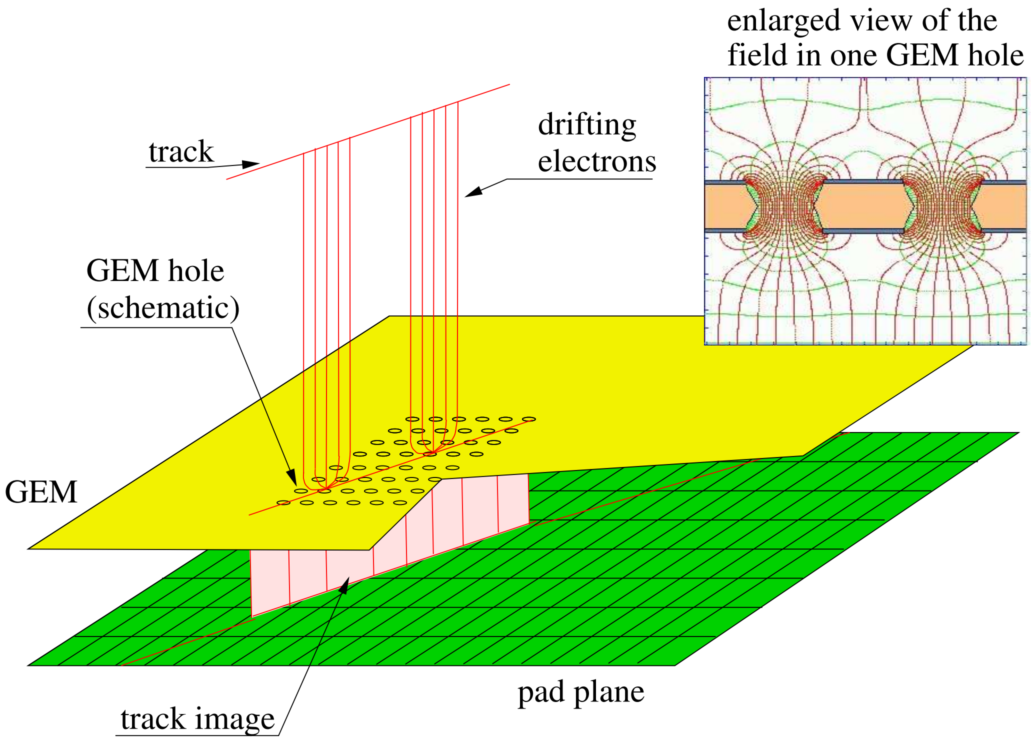

Figure 15: Effect of a GEM plane on the charge collection towards the pad plane of a TPC [10].

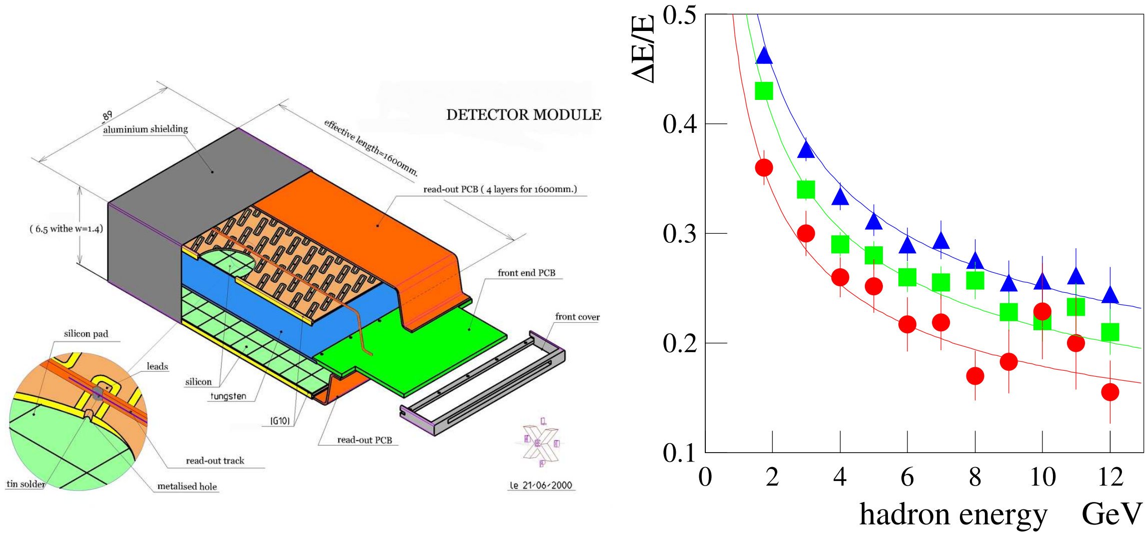

Figure 16: Calorimetry options of the TESLA proposal [10]. On the left: scheme of the slab proposed as the basic component of a Si-W electromagnetic calorimeter. On the right: resolution in the hadron calorimeter energy obtained by using: the deposited energy in the scintillation material (blue triangles), the pad multiplicity (green squares), and the full digital structure (red dots).

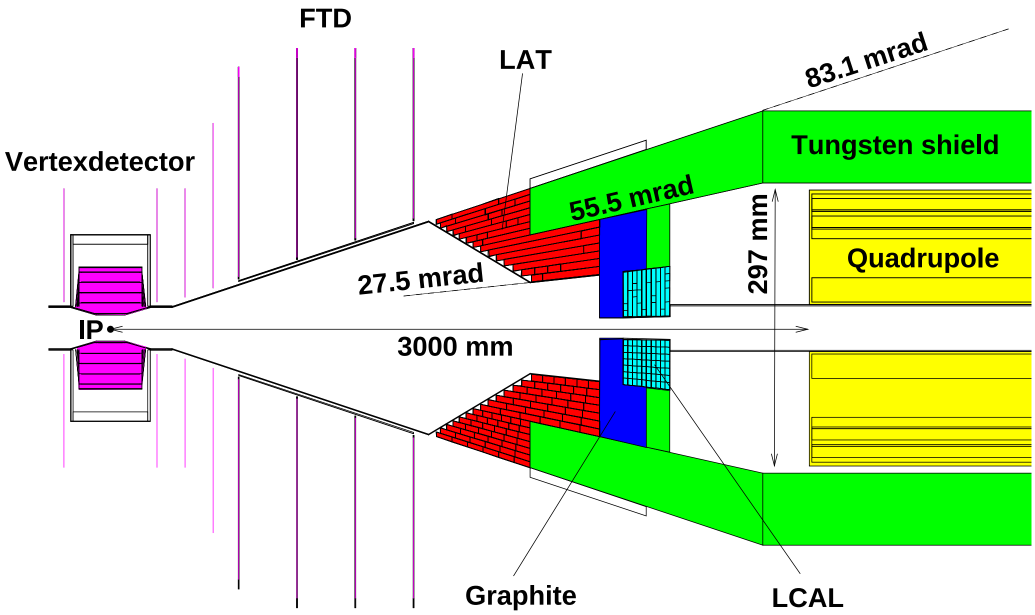

Figure 17: Mask layout [10] for the TESLA proposal (LCAL: luminosity detector, LAT: low angle tagger, FTD: forward tracking detectors).

there will be no such a system. The low repetition rate (5 Hz) leads to a separation between trains of 200 ms, enough to make any decision on the basis of full event analysis. The only point under discussion is the necessity or not of installing an intermediate event builder system at the subdetector level [10].

4 Higgs Physics

The most important problem that Particle Physics will face in the next future is the understanding of the origin of the symmetry breaking mechanism in the electroweak sector. To date, there is no evidence of the existence of the Higgs particle predicted by the SM, and it could well happen that a different mechanism turns out to be the ultimate responsible of the rich particle spectra observed in Nature.

There are some hints pointing to a low mass Higgs particle as the most coherent solution to the puzzle. In Figure 18 we show some theoretical constraints as well as the present experimental limits on the Higgs mass, m_{H}. On the left figure, the white region represents the SM permitted range of masses as a function of the energy scale, Λ [15]. Only m_{H} values in a restricted range are allowed if the SM has to be kept as an unmodified theory up to the Planck scale (10^{19} GeV). For instance, a value of $m_{\mathrm{H}} = 100$ GeV would necessarily imply the existence of new physics beyond the SM above the physics scale of 100 TeV. The excluded lower region represents the sets of values for which the asymmetric vacuum minimum required in the spontaneous symmetry breaking mechanism does not exist. The excluded upper region corresponds to values for which the potential of the theory can go to $-\infty$, and the theory becomes "trivial". These calculations are performed in a perturbative way, but lattice calculations also confirm that high m_{H} values do not lead to a reasonable SM behaviour. In both Figures we can observe the experimental upper limits on the Higgs mass. On the right figure we observe the evolution of the χ^2 of the experimental fit [16], as well as the lower limit band from direct searches. The second curve in the same figure illustrates the fact that the dominant uncertainty comes from the limited accuracy in the determination of α_{QED} at the scale of the Z mass [16]. From these figures one is tempted to conclude that a Higgs mass in the range 110-200 GeV is favoured by the data. However, one must keep in mind that all constraints (including the experimental ones) are determined on the assumption of a pure SM scenario.

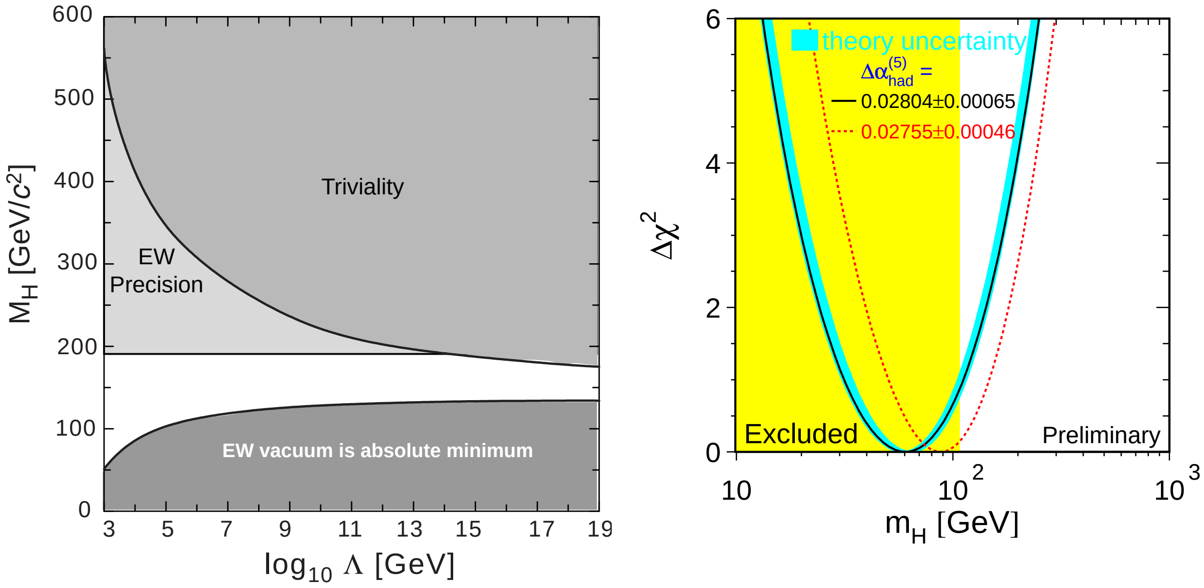

Figure 18: Indirect theoretical constraints [15] (left) and direct experimental limits [16] (right) on the Higgs mass. All curves and limits shown are only valid in the framework of the Standard Model.

Nevertheless, one can not ignore the previous hints, specially when Nature seems to follow the SM predicted behaviour at the electroweak scale. In addition, many of the models favoured by theorists (like supersymmetry) predict Higgs masses in that range or even below 150 GeV. A program for a Higgs study and search in the range 110-200 GeV is therefore of the outmost importance for an e^+e^- TeV linear collider machine, whereas one of the critical questions is what kind of useful information can a post-LHC e^+e^- collider add. We will try to answer this question in the following subsections.

4.1 Mass measurement

At LEP energies ($\sqrt{s} \approx 200$ GeV) the dominant Higgs production mechanism is "Higgs-strahlung": $e^+e^- \rightarrow Z^* \rightarrow ZH$. At higher energies, this process starts to compete with the fusion mechanism: $e^+e^- \rightarrow W^*W^* \rightarrow e^+e^-\nu_e\overline{\nu}_e$ (Figure 19), although the existence of energy-momentum constraints favours the Higgs-strahlung channel as the optimal one in terms of cleanest signal and precision physics capabilities. Concerning branching fractions, the dominant channels are $H \rightarrow b\bar{b}$ and $H \rightarrow WW^{(*)}$, depending on the exact value of m_H (Figure 20). At masses $m_H \lesssim 2m_W$ the Higgs width is small compared to the experimental resolution and a precise measurement of the total width from the mass distribution is not possible.

Very attractive from the physical point of view is an inclusive measurement of the total mass spectra in the $e^+e^- \rightarrow \mu^+\mu^- X$ channel. Just requiring consistency with the Z mass for the $\mu^+\mu^-$ system and thanks to an acceptance almost independent of X, the full Higgs-strahlung cross section can be measured. This gives access to an estimate of the HZZ coupling (and therefore of

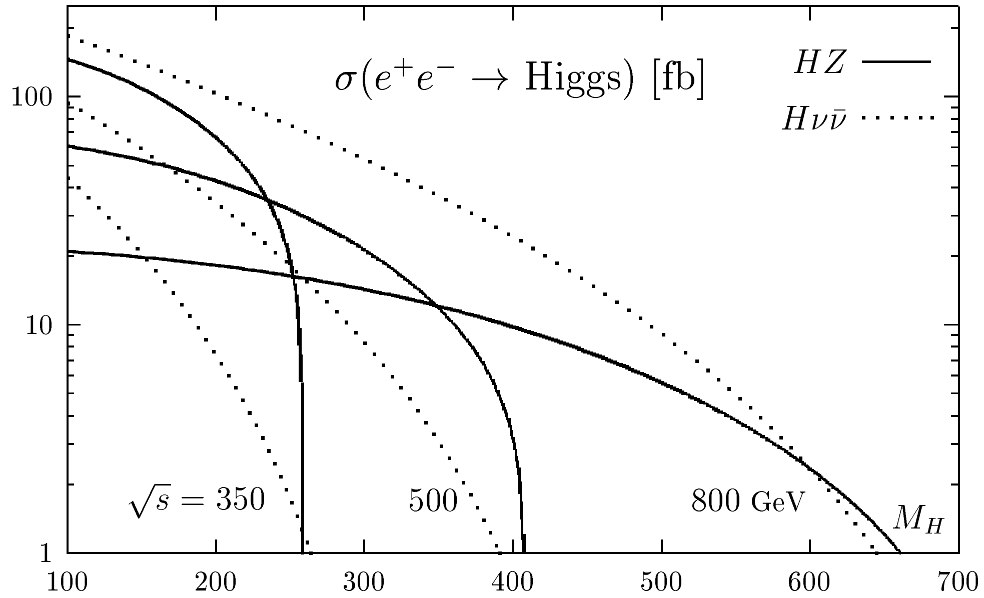

Figure 19: Contribution of Higgs-strahlung and WW-fusion Higgs production processes as a function of the center-of-mass energy, $\sqrt{s}$.

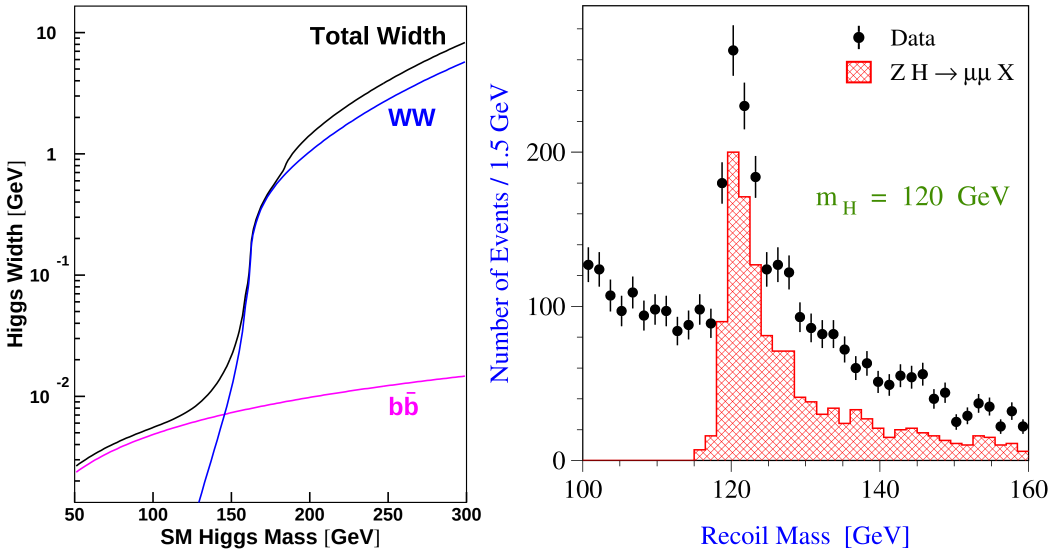

Figure 20: Properties of the Higgs particle. Left: partial and total widths of the SM Higgs particle as a function of its mass m_{H}. Right: expected distribution of the recoil mass in the inclusive process $e^+e^- \to \mu^+\mu^- X$ for $m_{\mathrm{H}} = 120$ GeV [7]. The acceptance (TESLA option) turns out to be almost independent of X.

$\Gamma(H \to ZZ)$), independent of the Higgs branching fractions. The recoil mass spectra is shown in Figure 20.

The best mass resolution is obtained by a dedicated study of the $e^+e^- \to HZ \to b\bar{b}q\bar{q}$ channel. Important ingredients in the analysis are: energy-momentum conservation constraints, consistency with the Z mass for the $q\bar{q}$ system and a correct description of beamstrahlung effects. Final resolutions on m_H of the order of 50 MeV are expected.

4.2 Branching fractions and total width

Figure 21a shows TESLA simulated results as a function of the Higgs mass compared to the SM expectations. The good performance in terms of resolution and particle identification leads to measurements of few percent precision in all cases. The physics potential is better illustrated in Figure 21b. A simultaneous measurement of the $H \to b\bar{b}$ and $H \to c\bar{c}$ branching fractions provides sensitivity to MSSM scenarios even if the m_A mass lies above 600 GeV.

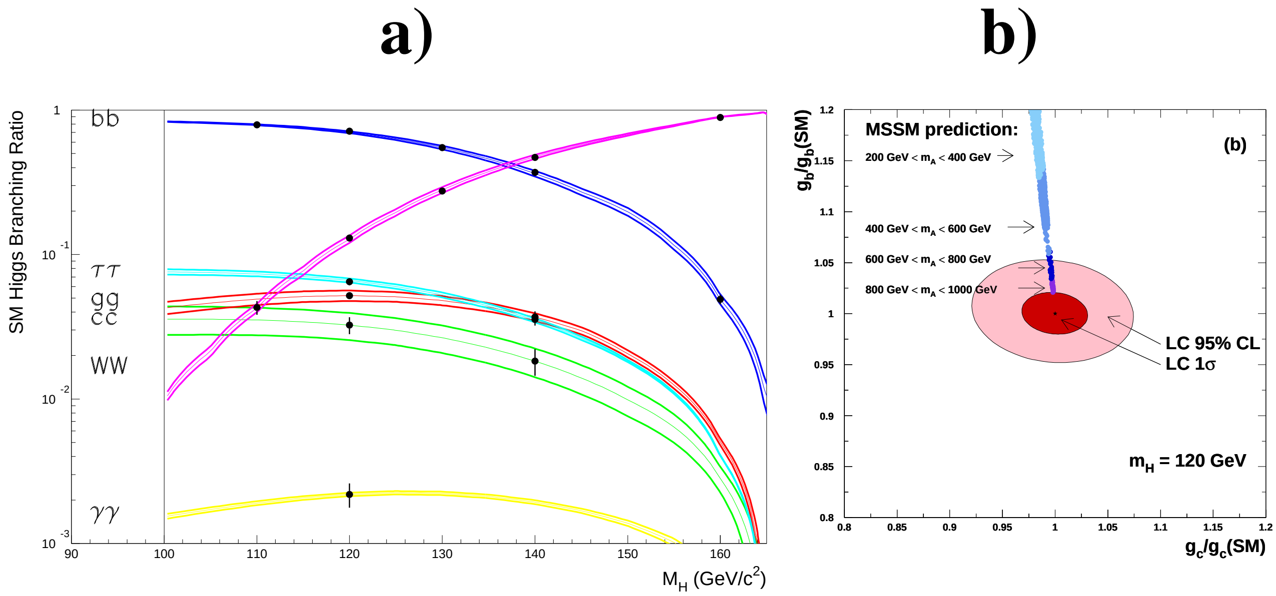

Figure 21: Sensitivity to new physics scenarios via the measurement of Higgs branching fractions [7]. Figure a) shows the expected experimental precision (of few percent in all cases) compared to the SM predictions. Figure b) illustrates the sensitivity in the specific case of the MSSM. A precise measurement of the $H \to b\bar{b}$ and $H \to c\bar{c}$ decay channels is sensitive to m_A masses above 600 GeV.

Since the total width of the Higgs particle, Γ_H, will probably be much smaller than the experimental mass resolution, a simultaneous measurement of the branching fraction and partial width into a specific final state is necessary. The most promising option for Higgs masses $m_H \geq 120$ GeV is the WW^* final state, where by WW^* we denote the case in which only one of the W bosons has a resonant behaviour: $WW^* \to Wf\overline{f}'$, relevant for Higgs masses below the WW threshold: $m_H \lesssim 2m_W$. The large value of the Higgs coupling to the weak bosons guarantees a sizeable statistics for masses as low as $m_H = 120$ GeV. The total width can be determined as follows:

$$\Gamma_H = \frac{\Gamma_{WW^*}}{Br(H \to WW^*)}$$

Γ_{WW^*} can will extracted from the WW fusion cross section (Figure 22a), whereas the direct access to the WW^* final state will provide $Br(H \to WW^*)$ (Figure 22b).

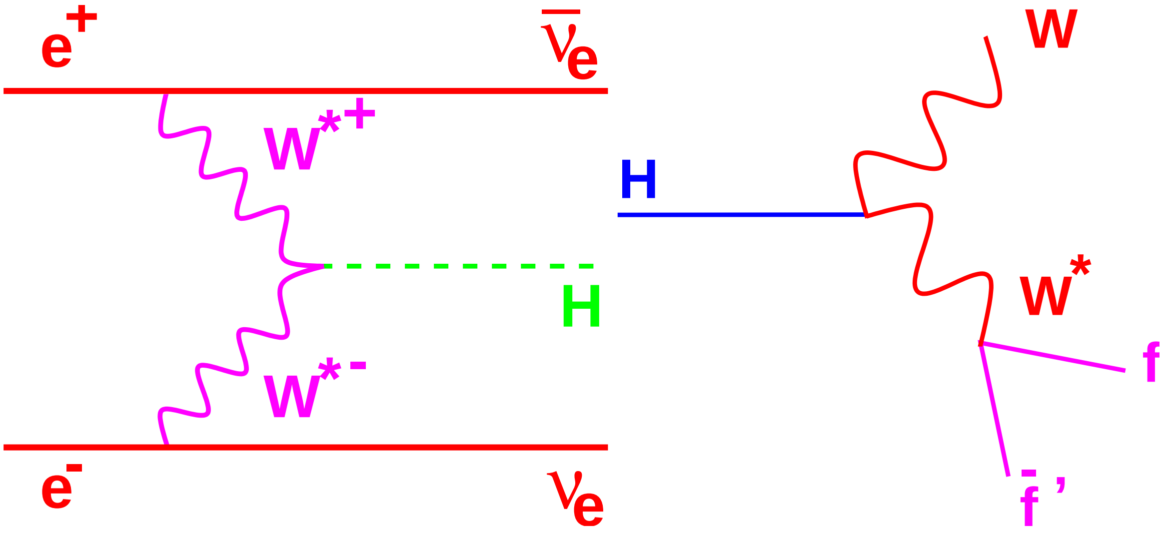

Figure 22: Processes leading to an optimal measurement of the total SM Higgs width for $m_H \gtrsim$ 120 GeV. Left: WW-fusion process, providing information on the HWW coupling. Right: $H \to WW^{(*)}$ decay, providing information on the relative weight of the $HWW^{(*)}$ decay with respect to the total decay width.

The WW-fusion cross section can be extracted from an analysis of the missing mass distribution in $e^+e^- \to WW\nu\bar{\nu}$ events (Figure 23). Higgstrahlung events concentrate on the missing mass region around m_Z, and are clearly distinguishable from the WW-fusion signal, which presents a broad spectrum peaking at larger masses. Assuming a center-of-mass energy of 500 GeV and an integrated luminosity of 500 pb^{-1}, a relative resolution of 6% seems attainable for a SM Higgs in the range 120 GeV $< m_H <$ 160 GeV.

An alternative method to measure the total Higgs width is substituting the measurement of the WW-fusion cross section by the measurement of the total Higgs-strahlung cross section. The latter gives access to the HZZ coupling, which is related to the HWW coupling by $SU(2)_L \times U(1)_Y$ symmetry considerations, difficult to violate (in a sizeable way) by physics signals beyond the SM. This method leads to a measurement of Γ_H with similar precision. One could think on the possibility of determining Γ_H from the coupling of the Higgs to photons: $\Gamma_H = \Gamma_{\gamma\gamma}/\text{Br}(H \to \gamma\gamma)$. Unfortunately, and even if the $H\gamma\gamma$ coupling gets accurately determined in $\gamma\gamma$ collisions, the measurement is statistically limited to a precision of $\approx 20\%$. This is due to the small value of the branching fraction ($\sim 0.1\%$). The study of this decay channel is nevertheless important, since it proceeds via loops which are sensitive to physics beyond the SM.

Finally, there is the possibility of measuring the top-Higgs Yukawa coupling in a large range of Higgs masses. In the case of a light Higgs, $m_H \approx$ 120 GeV, preliminary studies at $\sqrt{s}$ = 800 GeV and large luminosities ($\mathcal{L} = 1\ \text{ab}^{-1}$) show that a precision of 10% or better can be reached via the $e^+e^- \to t\bar{t}H$ associated process. If Nature prefers a Higgs with a larger mass, $2m_t < m_H \lesssim$ 500 GeV, then the WW-fusion process $e^+e^- \to W^*W^*\nu\bar{\nu} \to H\nu\bar{\nu} \to t\bar{t}\nu\bar{\nu}$ will provide a measurement of similar precision (Figure 23).

4.3 Other Higgs properties

Concerning the Higgs properties which can be optimally studied at the linear collider, it seems important to proof that the responsible of the electroweak symmetry mechanism really corresponds to a 0^{++} state. Parity can be investigated via the differential cross section of the $e^+e^- \to ZH$

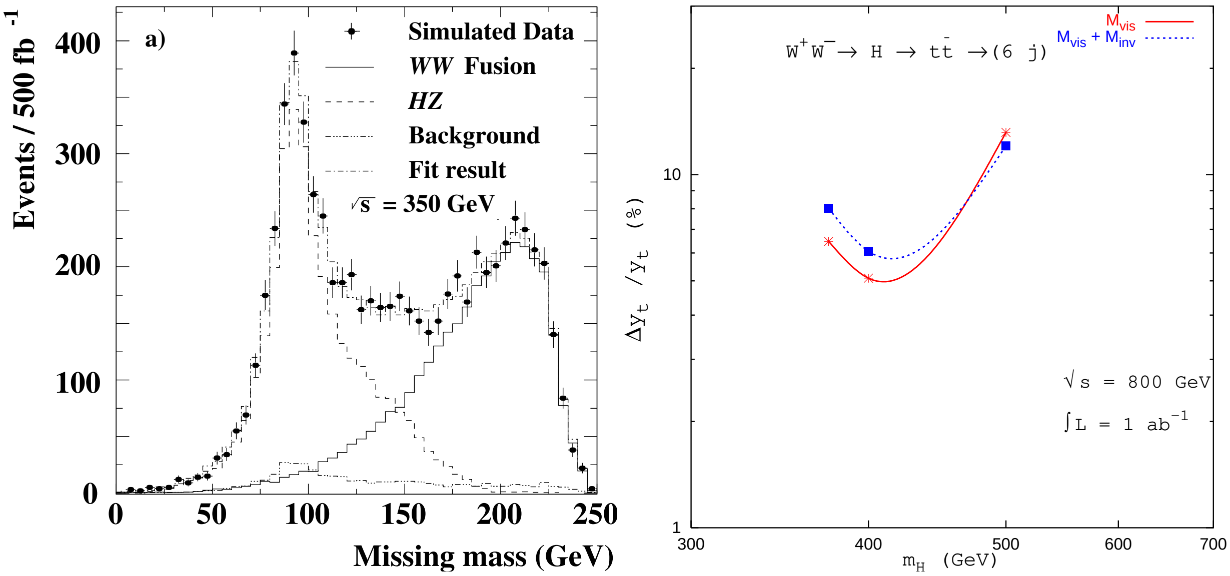

Figure 23: Left: measurement of the WW-fusion cross section at the linear collider [7]. The missing mass spectrum is enough to disentangle Higgs-strahlung and WW-fusion contributions. Right: measurement of the Higgs-top Yukawa coupling for large Higgs masses via the WW-fusion process [17]. This latter measurement will be extremely difficult at the LHC.

process as a function of the Higgs polar angle. A pseudoscalar admixture of $e^+e^- \to ZA$ leads to a different distribution, more peaked at low polar angles. The spin of the particle can be cleanly determined by a threshold scan of the Higgs-strahlung cross section (Figure 24). Just 20 pb^{-1} per energy point seem to be enough to exclude $J = 1$ and $J = 2$ possibilities.

Another fundamental analysis at the linear collider is the measurement of the Higgs self-couplings. Once the Higgs has been found, all parameters in the Higgs potential, $V(H) = \lambda v H^2 + \lambda v H^3 + \frac{1}{4} H^4$ get fixed. It is therefore important to test this sector, intimately related to the spontaneous symmetry breaking mechanism of the SM. Preliminary studies at TESLA show that, although difficult, a precision of 15% on the triple self-coupling, λv, could be reached, via the $e^+e^- \to ZHH$ process.

4.4 Higgs summary. Comparison with the LHC

Under the most likely assumption of a light Higgs particle, the physics potential of the linear collider is summarized and compared to the LHC in Table 4. All measurements quoted in the Table are extremely important. Finding the Higgs particle and measuring its mass represents by itself a key test of the validity of the SM. The LC will certainly measure it with a precision better than one per mille. A precise determination of the total Higgs width may provide hints of the existence of invisible, anomalous or unexpected decays, thus signalling the presence of new physics beyond the SM. Whether the LHC can provide a sensible measurement of the total width of a light Higgs is still under study. As explained in previous sections, an accurate measurement of all partial widths will help in pointing to the model lying beyond the SM and represents an important test of the connection between spontaneous symmetry breaking mechanism and particle masses. Only some of the partial widths will be accessible at the LHC. Determining the Higgs quantum numbers and studying the shape of the Higgs potential in the SM remain unique features of the LC.

It is therefore evident that the LC will play a complementary role with respect to the LHC in the Higgs sector. LHC will discover the Higgs and study many of their properties with a

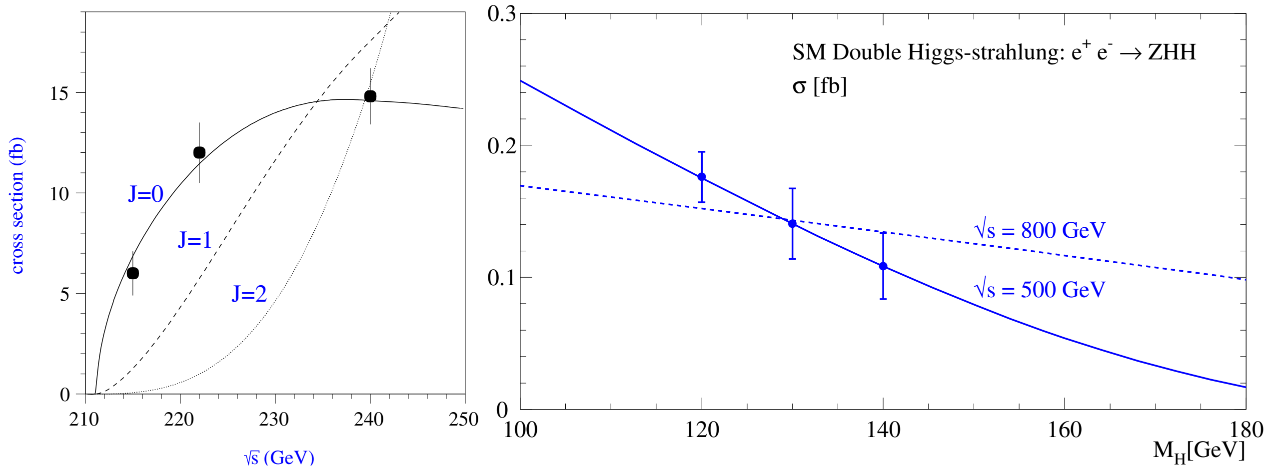

Figure 24: Measurement of Higgs properties at TESLA [7]. Left: measurement of its spin by threshold scan of the Higgs-strahlung cross section. Right: measurement of the triple self-coupling of the Higgs via the $e^+e^- \to ZHH$ process.

reasonable precision, and the LC will be the machine who will study it in great detail, aiming to a better understanding of the electroweak symmetry breaking mechanism.

Table 4: Summary table with the expectations at the LC and at the LHC in the analysis of a light SM Higgs boson. Precisions are relative and given in percent.

Measurement	Precision at the LC	At the LHC
$m_{\rm H}$	$\approx 0.05\%$	$> 0.1\%$
$\Gamma_{\rm H}$	6%	under study
Partial widths	few %	only some are accessible
Spin and parity	OK	?
Trilinear self-coupling	15%	?

5 Beyond the SM

Another important point in the physics program of the linear collider is the search for new physics beyond the SM. Within the best theoretical and phenomenologically motivated scenarios we find the so called "supersymmetric" (SUSY) models [18]. In its simplest implementation, the Minimal Supersymmetric Standard Model (MSSM), the number of fundamental particles in Nature gets duplicated (one boson for each existing fermion and viceversa) and two Higgs doublet fields are required (see Table 5).

It is well known that SUSY at the TeV scale is one of the best candidates to solve many of the theoretical problems that the SM faces at very high energies. The price to pay is the inclusion in the study of many new free parameters and problems. Since the most probable SUSY scenario at the LC startup is the existence of hints at the LHC, the best approach is to show the LC potential from qualitative arguments and minimally model-dependent examples.

The main reason to support a strong SUSY physics program at the LC is shown in Figure 25. The figure shows the typical spectra of supersymmetric partners in three typical MSSM symmetry breaking scenarios considered: mSUGRA (Supergravity mediated), GMSB (Gauge Mediated

Table 5: Particle content in the MSSM. For each known type of particle ($q, \ell, \nu, W^{\pm}, Z, \gamma, g$) there must exist a supersymmetric partner ($\tilde{q}, \tilde{\ell}, \tilde{\nu}, \tilde{\chi}^{\pm}, \tilde{\chi}^0, \tilde{g}$), with its spin differing in $\frac{1}{2}$ unit. Two Higgs doublet fields are necessary in this minimal model. Weak and mass eigenstates do not coincide in general, and the structure of mixing matrices may be largely different in the supersymmetric sector.

	Spin 0	Spin $\frac{1}{2}$ Weak eigenstates	Spin $\frac{1}{2}$ Mass eigenstates	Spin 1
Matter	$\tilde{\nu}$	ν_{MNS}	ν	
	$\tilde{\ell}$	ℓ_{MNS}	ℓ	
	$\tilde{q}$	q_{CKM}	q	
Interactions		$\tilde{g}$		g
	$H^{\pm}$	$\tilde{H}^{\pm}, \tilde{W}^{\pm}$	$\tilde{\chi}_i^{\pm}$	$W^{\pm}$
	h, H, A	$\tilde{h}_u^0, \tilde{h}_d^0, \tilde{W}^0, \tilde{B}^0$	$\tilde{\chi}_i^0$	Z, γ

SUSY Breaking) and AMSB (Anomaly Mediated SUSY Breaking). Assuming a center-of-mass energy of $\sqrt{s} = 500$ GeV at the LC, all states below the plotted band will be accessible. And it is almost evident that sleptons, neutralinos and charginos are clean targets for high precision spectroscopy studies in e^+e^- machines. In the following, and in order to simplify, we will only consider the mSUGRA case. Similar conclusions in what respects the LC physics potential can be obtained in the GMSB and AMSB scenarios.

5.1 MSSM spectroscopy and access to SUSY parameters

A typical, extremely clean, example is the production of smuons via the reaction $e^-_R e^+_L \to \tilde{\mu}_R \tilde{\mu}_R \to \mu^+\mu^-\tilde{\chi}_1^0\tilde{\chi}_1^0$. The study assumes that the neutralino $\tilde{\chi}_1^0$ is the lightest supersymmetric particle (LSP) and it is stable. The availability of longitudinally polarized beams (typically polarizations of 80% for electrons and 60% for positrons are considered) is critical in this case, since this choice ($e^-_R e^+_L$) highly suppresses the $e^+e^- \to WW \to \mu\mu\nu\nu$ background. In fact, the main background in the analysis is another SUSY reaction leading to the same final state (Figure 26). The end-points of the muon energy spectrum are related to the values of $m_{\tilde{\mu}}$ and $m_{\tilde{\chi}_1^0}$. By performing a threshold scan of the reaction, mass precisions of the order of 0.1% are obtained.

The search for charginos is cleanly performed through semileptonic plus missing energy final states: $e^-_L e^+_R \to \tilde{\chi}_1^+\tilde{\chi}_1^- \to \ell^{\pm}\nu\tilde{\chi}_1^0 q\overline{q}'\tilde{\chi}_1^0$. In this case the cross section is large and the WW background is not problematic. By analyzing the energy of the di-jet system (Figure 27) mass resolutions of the order of 200 MeV seem attainable. This polarization choice preferentially selects the $\tilde{W}$ component of the chargino mass eigenstate (see the diagram in Figure 27). In fact, varying the beam polarizations gives access to the $\tilde{W}^{\pm} - \tilde{H}^{\pm}$ mixing matrix in the chargino sector. This matrix depends on fundamental parameters of the MSSM. Preliminary studies show precisions on the parameters μ and M_2 of the order of 1% [7].

A similar treatment is possible in the case of the neutralino sector. An analysis of the reaction $e^-_L e^+_R \to \tilde{\chi}_2^0\tilde{\chi}_2^0 \to \ell^+\ell^-\tilde{\chi}_1^0\ell^+\ell^-\tilde{\chi}_1^0$ leads to a measurement of the neutralino masses with precisions in the 150 − 300 MeV range. In this case, a study as a function of the beam polarization gives access to the (more complicated) neutralino mixing matrix and in particular to the M_1 parameter (associated to the $U(1)_Y$ group and therefore not accessible in the chargino analysis).

5.2 SUSY searches: comparisons with the LHC

So far, we have not considered many other interesting SUSY analyses which can be performed

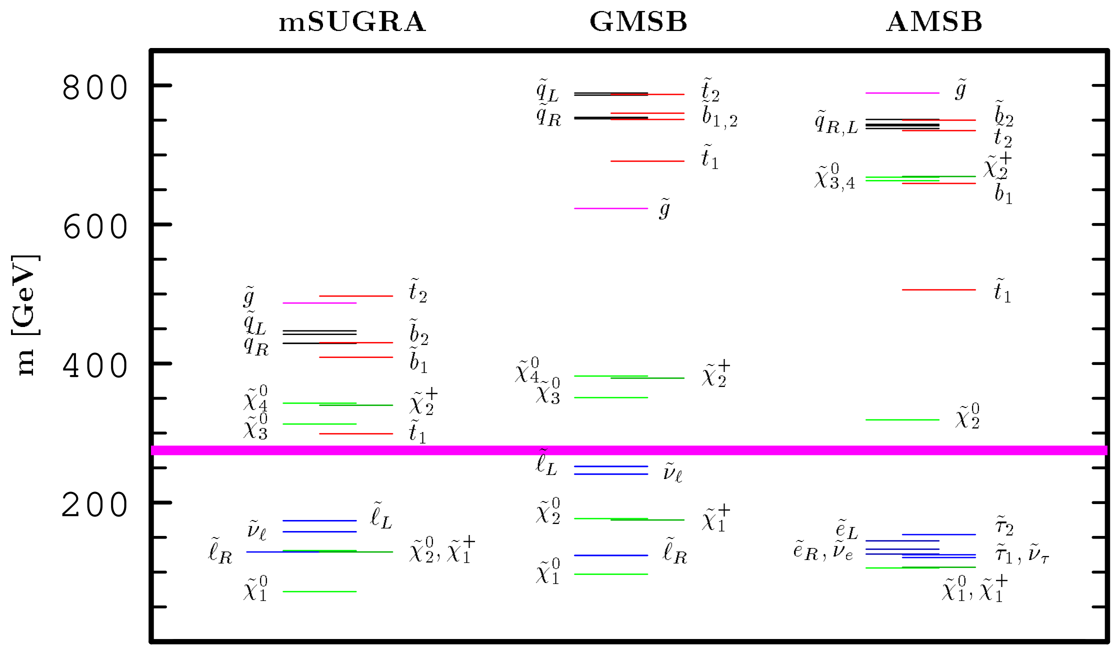

Figure 25: Spectrum of supersymmetric particles in three different MSSM supersymmetry breaking scenarios: mSUGRA, GMSB and AMSB. All the states below the horizontal band will be accessible at a e^+e^- linear collider with $\sqrt{s} = 500$ GeV.

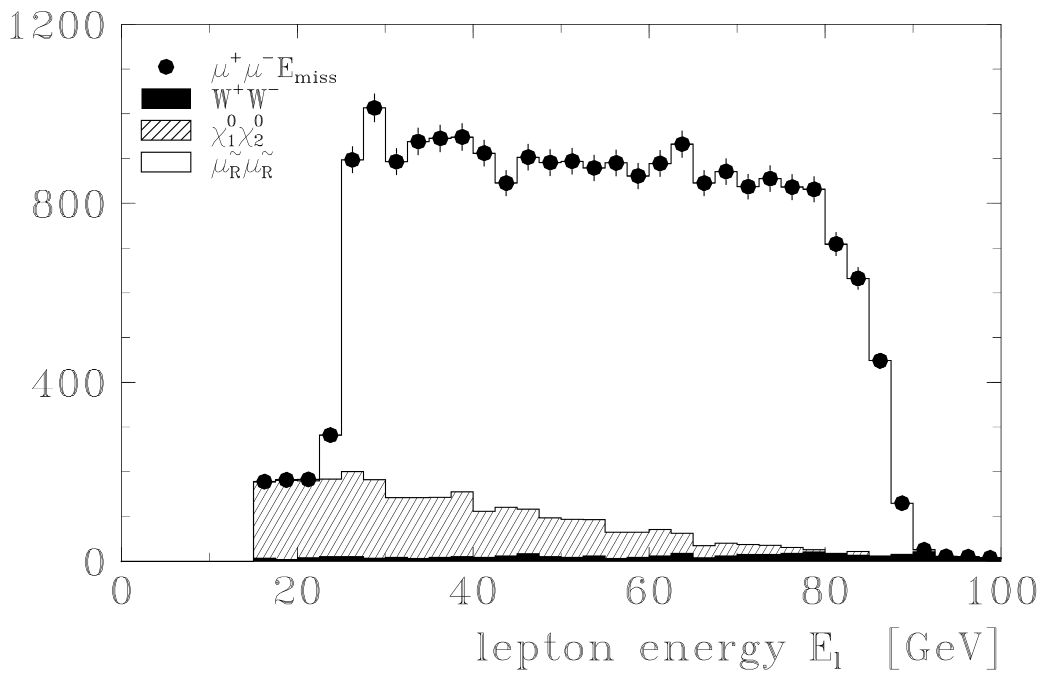

Figure 26: Spectrum of the muons energy in the process $e^-_R e^+_L \to \tilde{\mu}_R \tilde{\mu}_R \to \mu^+\mu^- \tilde{\chi}^0_1 \tilde{\chi}^0_1$ [7]. The main background corresponds to the process $e^-_R e^+_L \to \tilde{\chi}^0_1 \tilde{\chi}^0_2$, which may lead also to a final state with muons plus missing energy. The $e^+e^- \to WW$ is highly suppressed by the longitudinal polarization choice for the colliding electrons.

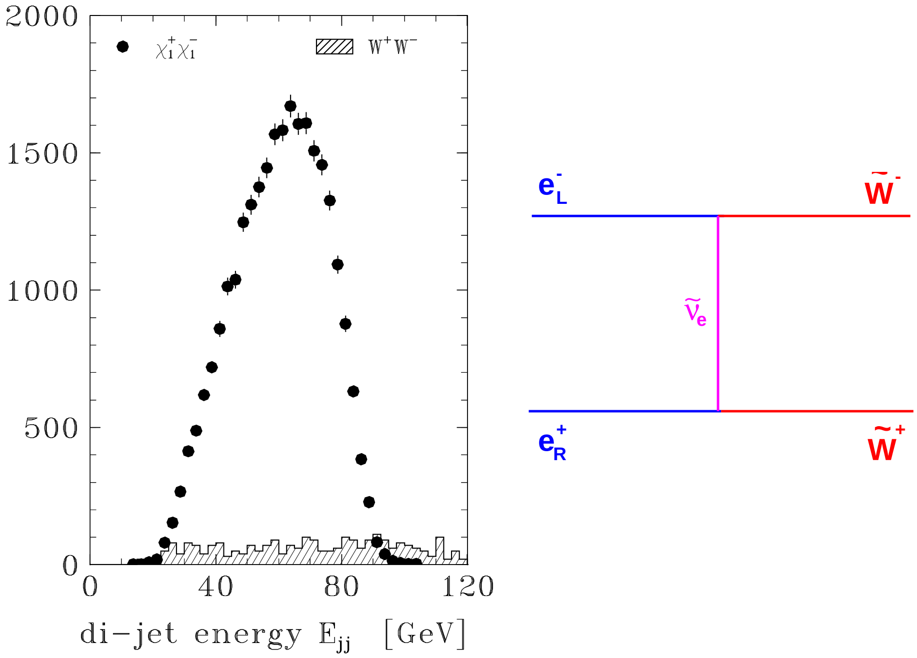

Figure 27: Left: distribution of the di-jet energy in the $e^-_L e^+_R \to \tilde{\chi}_1^+ \tilde{\chi}_1^- q\overline{q'}\ell$ + missing energy. Note the high rate of the SUSY signal as compared to the WW background. Right: diagram illustrating the fact that this polarization choice enhances the Wino component in the chargino final state.

at the LC: stop searches which may escape detection at hadron colliders, stau searches in large $\tan\beta$ scenarios, R-parity violation, use of eγ and $\gamma\gamma$ collider options, non-minimal SUSY models, … In any case, the few examples above show that LC and LHC are complementary machines in SUSY studies. Although the LHC discovery potential is larger in terms of kinematic reach, a big portion of the SUSY parameter space will be accessible at a LC with $\sqrt{s}$ in the 500 GeV – 1 TeV range:

- The LC provides a clean environment in which all kinematically accessible SUSY processes can be studied in detail.
- The LC is able to perform SUSY spectroscopy with a minimal dependence on model parameter assumptions.
- The LC will lead to the most precise measurements (masses and model parameters) in the slepton, chargino and neutralino sectors.

Whereas the LHC will be a machine with an enormous SUSY discovery potential, the LC will be able to specify the scenario beyond the SM.

5.3 Other possibilities beyond the SM

SUSY is not the only possibility for physics beyond the SM, and the LC physics program is certainly prepared for this case. Recently, models with extra dimensions in which gravity is predicted to be strong at the TeV scale (in order to solve the so-called hierarchy problem) have become popular [19]. In e^+e^- collisions, these effects are searched for in reactions involving real or virtual manifestations of the graviton. Real graviton production studies concentrate on the

$e^+e^- \to \gamma G$ process, where the graviton escapes detection. The left plot in Figure 28 illustrates the sensitivity to a low gravity scale of $M_D = 5$ TeV for various choices of the number of large extra dimensions. The right plot shows the effects of a scale of 2 TeV on the left-right asymmetry of b quarks. In this case the graviton manifests virtually through the $e^+e^- \to G^* \to b\bar{b}$ process, which has a minimal dependence on the number of large extra dimensions. The expected sensitivity reach for this analysis at $\sqrt{s} = 500$ GeV is $M_D \lesssim 5$ TeV.

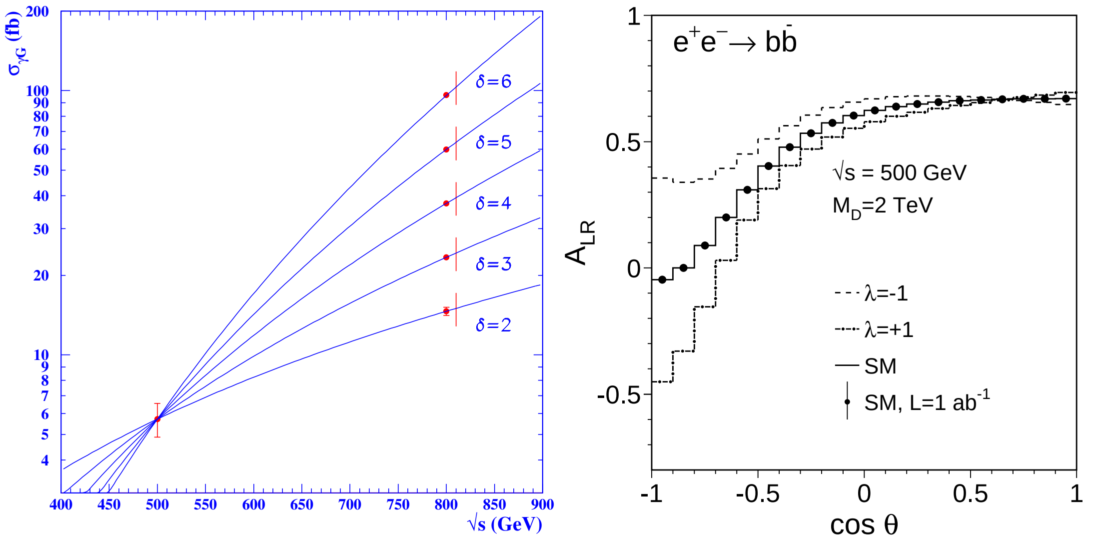

Figure 28: LC sensitivity to models with gravity propagating in large extra dimensions [7]. Left: evolution as a function of $\sqrt{s}$ of the $e^+e^- \to \gamma G$ cross section at a gravity scale of $M_D = 5$ TeV. Two measurements at different center-of-mass energies ($\sqrt{s} = 500$ GeV and $\sqrt{s} = 800$ GeV) with 500 fb^{-1} integrated luminosity are enough to find out the number of extra large dimensions associated to gravity. Right: sensitivity to low scale gravity scales through the analysis of the left-right asymmetry in $b\bar{b}$ events. The histogram with dots corresponds to the SM predictions. The effects of a virtual graviton in the $e^+e^- \to G^* \to b\bar{b}$ process at the scale of 2 TeV are easily distinguishable.

Another scenario beyond the SM would be the case in which a light, fundamental Higgs scalar is not found. In this case, the longitudinal components of the weak bosons will lead to interactions which diverge at large energies, like $e^+e^- \to W^*W^*\nu_e\bar{\nu}_e \to WW\nu_e\bar{\nu}_e$. An analysis of these type of reactions at $\sqrt{s} = 800$ GeV and high luminosity (1000 fb^{-1}) will provide sensitivity to new terms originating from physics scales in the $2-3$ TeV range. Strong WW interactions can also be investigated through their indirect effects on WWZ, WWγ triple gauge couplings. Moreover, strong scattering effects will modify the $e^+e^- \to WW$ cross section by means of a complex form factor F ($F = 1$ in the SM). Figure 29 illustrates the sensitivity on this factor at a LC with $\sqrt{s} = 800$ GeV and a luminosity of 500 fb^{-1} [20] for different strong scattering scenarios: LET (Low Energy Theorem, the limit case when neither Higgs nor new physics manifests at the TeV scale) and the presence of a vector resonance created by the new TeV scale binding forces. All cases are easily identified at the LC, with a precision comparable or better than that of the LHC.

The last scenario corresponds to the case in which a light Higgs exists and no evidence for new physics beyond the SM at the TeV scale is found. In this case, one has to exploit precision measurements. The most sensible option is searching for tiny deviations in total and differential cross sections in the $e^+e^- \to f\bar{f}$ process. New physics interactions at very high energies will most probably manifest via $e^+e^- f\bar{f}$ contact interactions. A linear collider operating at $\sqrt{s} = 500$ GeV with $\mathcal{L} = 1$ ab^{-1} will be sensitive to physics scales $\Lambda \gtrsim 40$ TeV, depending on the specific type of contact term involved [21]. This again leads to better limits than those expected at the LHC for

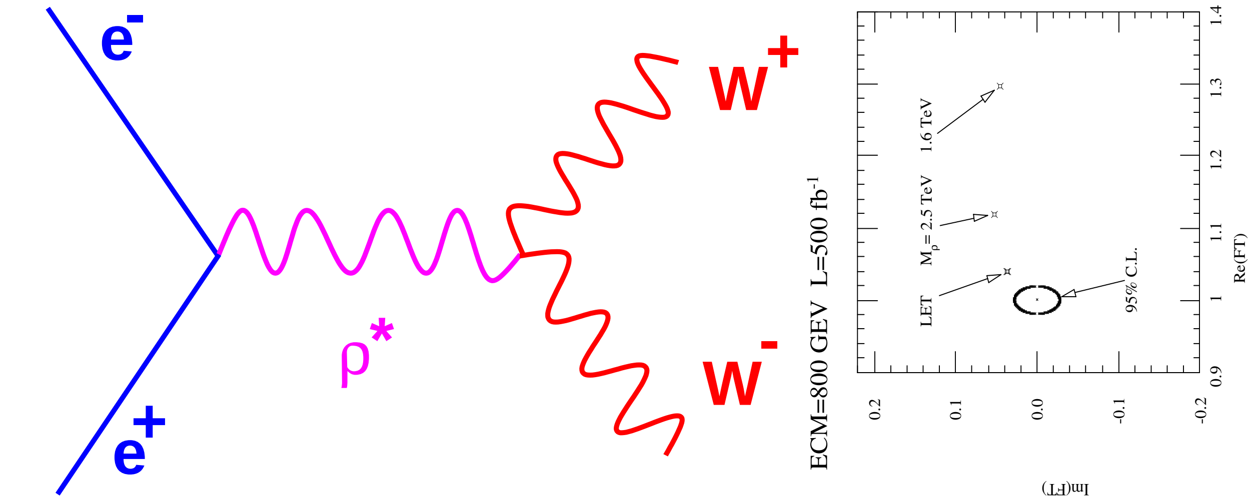

Figure 29: Left: Measurement of the global form factor affecting the $e^+e^- \to WW$ at the LC in the presence of different strong WW scattering scenarios (LET and vector resonance exchange). The ellipse around the SM value ($FT = 1$) denotes the expected 95% confidence level sensitivity of a measurement at $\sqrt{s} = 800$ GeV with an integrated luminosity of 500 fb^{-1} [20]. The right diagram illustrates the case of the exchange of a vector resonance, bounded through new forces appearing at the TeV scale.

100 fb^{-1} integrated luminosity.

6 Precision Physics

It is well known that e^+e^- collisions are clean environments to perform precision measurements. The LC offers four $\sqrt{s}$ regions particularly interesting:

- The high luminosity of the machine ($\mathcal{L} \gtrsim 10^{34}\ \mathrm{cm^{-2}s^{-1}}$) permits the collection of huge samples at the Z pole ($\approx 10^9$ Z decays, the *Giga-Z* option).
- In the same spirit, large samples of $e^+e^- \to WW$ events can be collected at the WW threshold, leading to an improved measurement of the W mass.
- There is the opportunity of performing precision top physics at the $t\bar{t}$ threshold ($\sqrt{s} \approx$ 350 GeV).
- Precision measurements at the nominal center-of-mass energy of the machine: $\sqrt{s} = 500$ GeV–1 TeV.

6.1 The Giga-Z option

A sample of 10^9 Z decays offers a unique physics opportunity. The question is: in which areas can the LC Giga-Z sizeably improve LEP-SLD measurements? In general, in all areas where present measurements (based on $\approx 10^7$ events) are still dominated by statistical uncertainties. Typical examples are forward-backward and left-right asymmetries. Table 6 shows present (LEP/SLC/Tevatron) and future (LC) uncertainties for some relevant electroweak observables [7]. One order of magnitude improvement is expected in the measurement of the effective weak angle from asymmetry measurements in the leptonic and b-quark sectors. Other observables ($\alpha_s, N_\nu, R_b, \rho_\ell$) may also get improved. No chance for m_Z, since beam uncertainties at the LC will be larger than those at LEP.

Table 6: Electroweak measurements at LEP/SLC/Tevatron compared to expectations for a GigaZ scenario at the LC [7]. The largest improvements are associated to the asymmetry measurements in the leptonic and heavy quark sectors.

Observable	LEP/SLC/Tevatron	LC precision
m_Z	91.1875 ± 0.0021	No improvement
$\alpha_s(m_Z^2)$	0.1183 ± 0.0027	$\pm\, 0.0009$
$\Delta\rho_\ell$	$(0.55 \pm 0.10)\ 10^{-2}$	$\pm\, 0.05\ 10^{-2}$
N_ν	2.984 ± 0.008	$\pm\, 0.0004$
R_b	0.21653 ± 0.00069	$\pm\, 0.00014$
$\sin^2\theta_{eff}^{lept}$	0.23146 ± 0.00017	$\pm\, 0.000013$
$\mathcal{A}_b$	0.898 ± 0.015	$\pm\, 0.001$

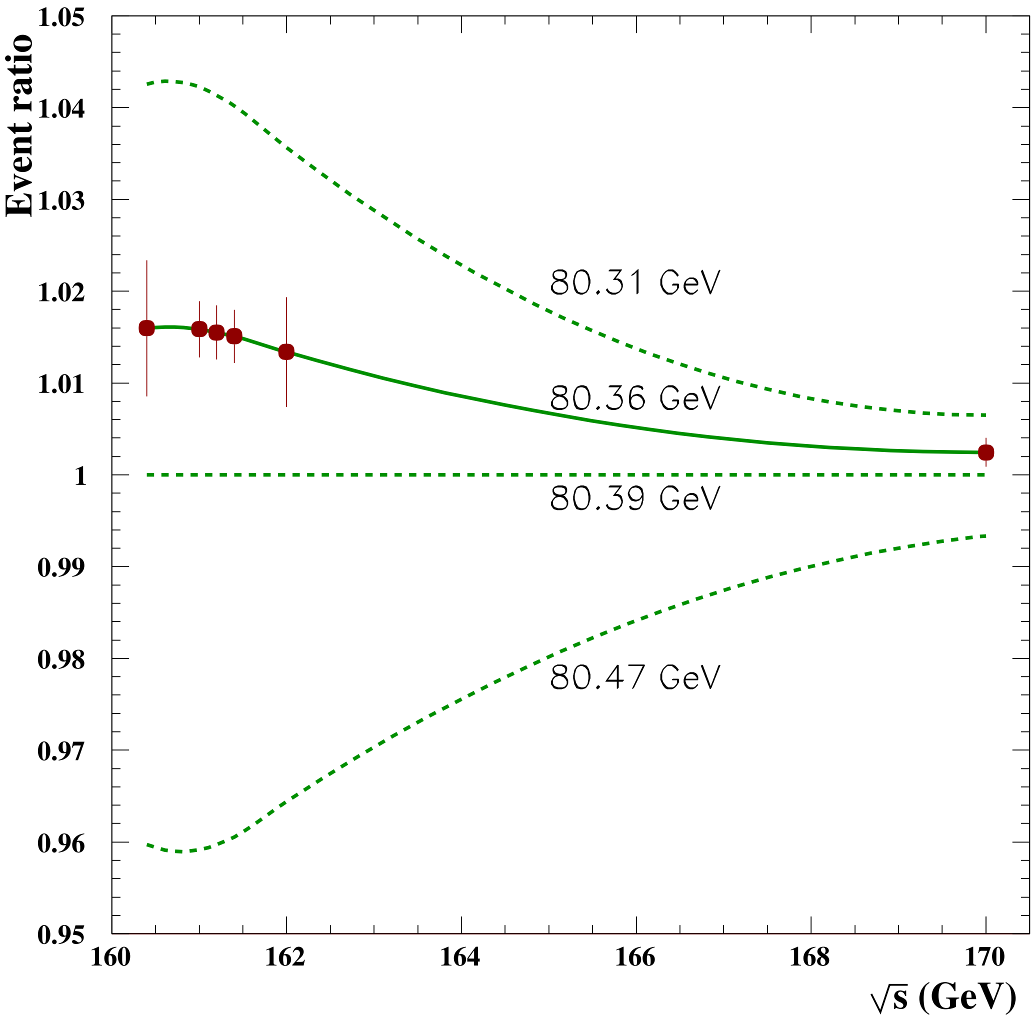

Figure 30: Measurement of the W mass at the LC (TESLA option). The analysis assumes an integrated luminosity of 100 $f\mathrm{b}^{-1}$ at the $e^+e^- \to WW$ production threshold. The accurate measurement of the cross section leads to an experimental uncertainty of $\Delta m_W \simeq 6$ MeV.

6.2 Running at the WW production threshold

Running at $\sqrt{s} \approx 161$ GeV gives the opportunity of performing an accurate measurement of the $e^+e^- \to$ WW cross section at threshold and, therefore, of the W mass. Although this method is free of many systematic errors, it was not the preferred one at LEP due to the lack of statistics. At the LC, an extremely precise measurement (with $\Delta m_{\rm W} \simeq 6$ MeV experimental error) seems feasible. The estimates for TESLA (Figure 30) assume an integrated luminosity of 100 $f\mathrm{b}^{-1}$. The ultimate uncertainty is difficult to predict, since present theoretical uncertainties at the threshold region are much larger than the quoted experimental uncertainty.

6.3 Top physics

A linear collider working at the threshold of $\mathrm{t\bar{t}}$ production is the ideal machine to perform precision measurements of the top quark properties. The top quark is also a unique component of the SM. Its large mass, of the order of the electroweak scale, makes it specially sensitive to the details of the electroweak symmetry breaking mechanism and to new physics effects in general. The program at the LC covers the precise measurement of its mass, width, form factors in production and decay, and the search of rare decays. Here we will concentrate on the mass and width measurements.

A physical manifestation of the large mass difference between the top quark and the other quarks is its huge width ($\Gamma_{\rm t} \approx 1.5$ GeV), much larger than the typical QCD scale ($\Lambda_{QCD} \sim 300$ MeV). Therefore, the top quark is expected to really behave like a *free quark*. It decays in a very short time, before feeling the strong forces necessary to form any hadronic resonance. QCD corrections can be safely taken into account in a perturbatively way.

The shape of the $e^+e^- \to \mathrm{t\bar{t}}$ production cross section versus $\sqrt{s}$ function at threshold is sensitive to the top quarks mass, as well as the differential cross section versus the top quark transverse momentum. The measurement of $m_{\rm t}$ is delicate by several reasons:

- From the experimental point of view, the threshold shape is largely affected by initial state radiation, beamstrahlung and machine effects (Figure 31 left).
- Theoretical effects due to higher order (NNLO) QCD corrections are not negligible. In fact, $m_{\rm t}$ and $\alpha_{\rm s}$ can be simultaneously determined by a fit to the experimental points, but a large correlation, depending on the definition of the top quark mass used in the calculations, may be present (Figure 31 right).

Despite these difficulties, statistical uncertainties of $\Delta m_{\rm t} \approx 50$ MeV and $\Delta\alpha_{\rm s}(m_{\rm Z}^2) \approx 0.0024$ are expected for an integrated luminosity of 100 fb^{-1}. Most of the theoretical uncertainties get absorbed in the $\alpha_{\rm s}$ measurement, and new theoretical calculations, aiming to a reduction of these errors, are under way.

The measurement of the top width $\Gamma_{\rm t}$ is based on a global fit to the total cross section, the forward-backward asymmetry and the differential cross section as a function of the top quark momentum. Preliminary studies ([22]) show that a relative precision of $\frac{\Delta\Gamma_{\rm t}}{\Gamma_{\rm t}} \approx 15\%$ is attainable.

6.4 Constraining new physics via precision measurements

The ultra-high precision measurements shown in the previous sections provide a unique tool to search for new physics beyond the SM. The accurate knowledge of $m_{\rm W}, m_{\rm t}$ and $\sin^2\overline{\theta}_{\rm W}$ leads to a precise prediction of the Higgs mass in the SM (Figure 32 left), which can be confronted to the direct measurement. From all this redundant information, the predictive power on new physics scenarios beyond the SM is remarkable. Figure 32 (right) is an example of the type of constraints that one can obtain in a SUSY scenario.

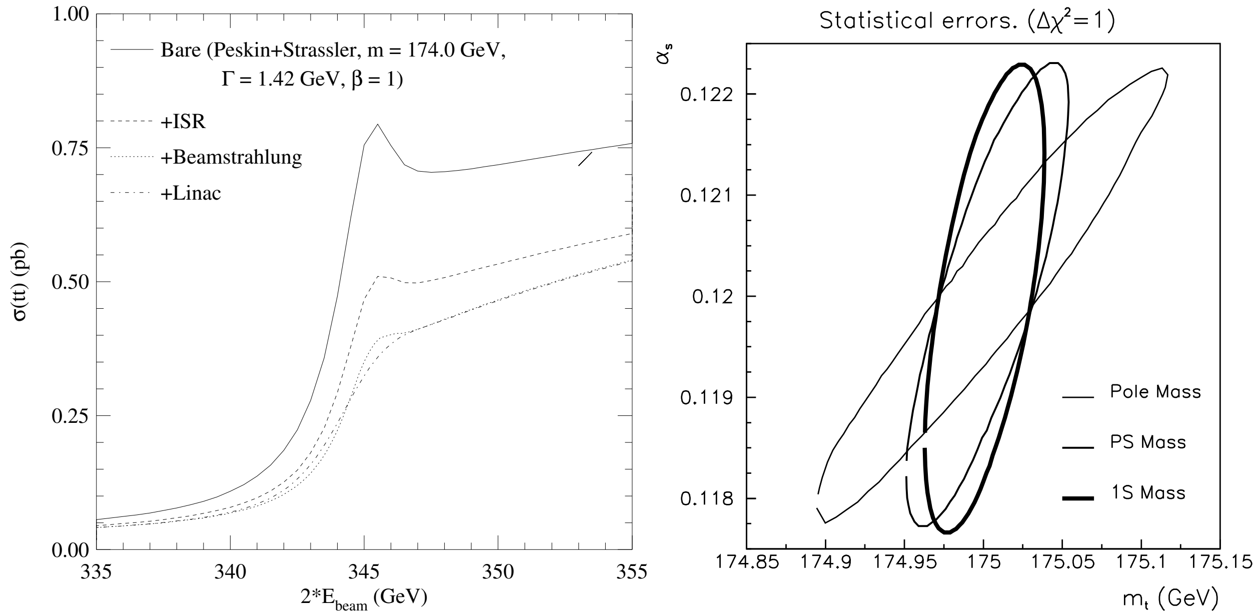

Figure 31: Top precision physics at the LC. Left: $e^+e^- \to t\bar{t}$ production cross section as a function of $\sqrt{s}$ at threshold. Distortions due to initial state radiation, beamstrahlung and accelerator effects are successively added to the bare prediction. Right: error contour from the simultaneous measurement of m_t and $\alpha_s(m_Z^2)$ at the LC [7]. Errors are statistical only. The results depend strongly on the mass scheme chosen for the theoretical (NNLO QCD) predictions.

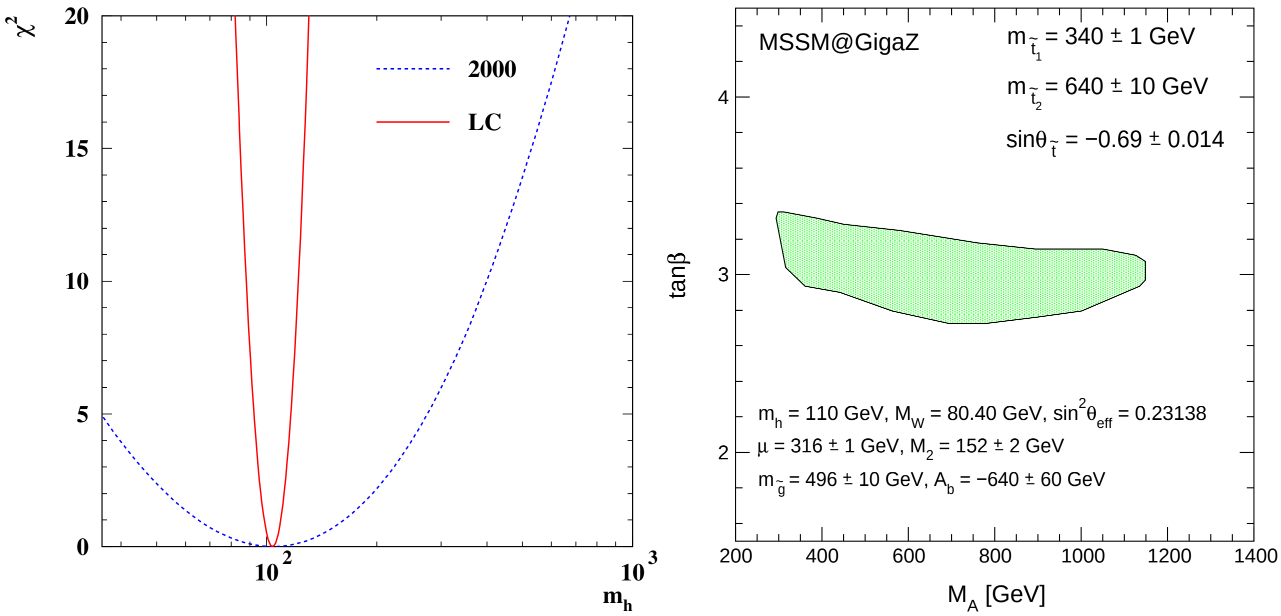

Figure 32: Left: Improvement in the determination on the Higgs mass at the LC based on precision measurements. Right: constrained region in the space of MSSM parameters assuming the existence of high precision measurements at the LC (m_W, m_t, $\sin^2\overline{\theta}_W$, …) [7].

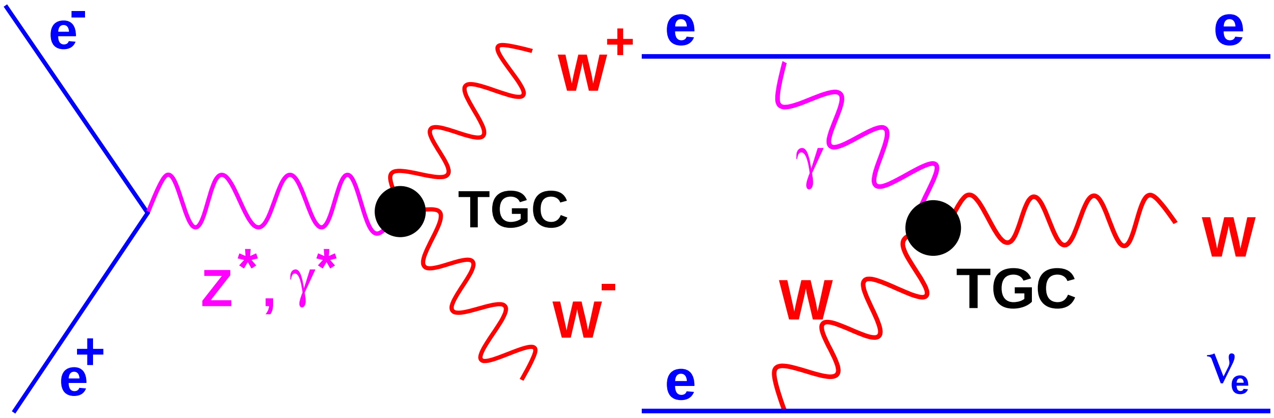

Figure 33: Diagrams containing anomalous WWZ and WWγ couplings. In the case of W-pair production at high energies, only the $e^-_L e^+_R$ helicity combination contributes to the SM process. For the SM single-W production process (right), only the $e^-_R e^+_L$ combination provides a negligible cross section. Therefore, using adequately polarized beams at the LC enhances the sensitivity to anomalous couplings.

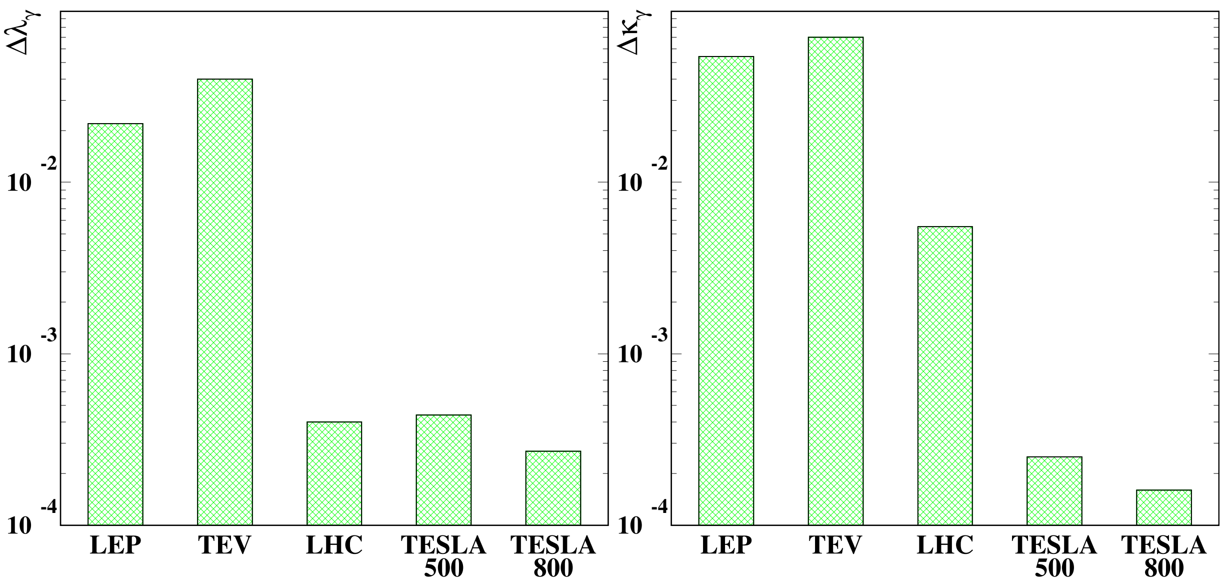

Figure 34: Precisions obtained and/or estimated in the measurement of anomalous triple gauge couplings at different accelerators (LEP, Tevatron, LHC and TESLA). The advantages of a LC (specially in the case of $\Delta\kappa_\gamma$) are clearly demonstrated.

6.5 Electroweak Physics at high energies

The accurate measurement of WWZ and WWγ triple gauge couplings (TGCs) is maybe the main point of the LC electroweak program at high energy. It is well known that deviations due to anomalous TGCs increase with the collision energy and, therefore, a LC working at the largest energies will be an optimal place to look for deviations. At very high energies ($\sqrt{s} \gg m_Z, m_W$) the SM reaction is almost dominated by V-A interactions (only $e_L^- e_R^+$ combinations contribute). In addition, the single-W process (Figure 33 right), having different helicity constraints and being the dominant component in Weν final states, is sensitive to WWγ anomalous couplings. It is evident that the use of adequate beam polarizations can help in enhancing the anomalous effects and in disentangling WWZ and WWγ anomalous components.

At the LC the high boost of the W bosons in the $e^+e^- \to$ WW process allows an accurate definition of their production polar angle, one of the most sensitive variables to anomalous couplings. In practice, the angular analysis can be almost performed by comparing to generator level predictions, since distortions due to detector resolution effects are small. As a result, anomalous deviations below 0.001 will be accessible (Figure 34). LHC and LC will therefore be the first machines able to measure and test the size of the radiative corrections to the WWZ and WWγ vertices (of the order of per mille in the SM and SUSY models, and larger in other scenarios beyond the SM).

7 Conclusions

Although this report is just a summary of the physics potential of future e^+e^- linear colliders, our hope is to have justified the necessity of such a physics program after the LHC era. The LC program is rich and certainly complementary to the LHC in almost any physics area. Independently of how the new signals manifest at the LHC -Higgs, SUSY, extra-dimensions, strongly interacting sectors, contact interactions- the LC will substantially contribute to the understanding of the physics at the new energy frontier and to the ultra-precise measurement of Higgs, top and electroweak particle properties. We do not want to forget other aspects which are unique to the LC, like the conception as an evolving and versatile facilities, or the useful intersections with other fields of science [13]. Certainly, the LC represents an opportunity which the High Energy Physics community should not miss.

8 Acknowledgements

The author wants to thank the Organizing Committee for their warm hospitality and help, as well as for the nice and relaxed atmosphere created at the meeting.

References

[1] LEP, *The LEP Design Report*, CERN Reports LEP/TH/83-29, LEP/84-01, AC/96-01.

[2] J. Ellis, E. Keil, G. Rolandi, CERN Preprint CERN-EP/98-03.

[3] R.R Assmann *et al.*, *A 3 TeV* e^+e^- *Linear Collider Based on CLIC Technology*, CERN-2000-008 (2000).

[4] The TESLA-N Collaboration, the ECFA/DESY LC Physics Working Group *et al.*, *TESLA Technical Design Report*, DESY 2001-011, ECFA 2001-23 (2001).

[5] The NLC Collaboration, *2001 Report on the Next Linear Collider*, SLAC-R-571, FERMILAB-Conf-01-075-E, LBNL-PUB-47935, UCRL-ID-144077 (2001).

[6] T. Abe *et al.*, *Linear Collider Physics Resource Book for Snowmass 2001*, SLAC-R-570, FERMILAB-Conf-01/058-E, LBNL-PUB-47813, UCRL-ID-143810-DR (2001).

[7] See TESLA Technical Design Report, Part III, *Physics at the* e^+e^- *Linear Collider*.

[8] N. Akasaka *et al.*, *JLC Design Study*, KEK-REPORT-97-1 (1997).

[9] M. Battaglia *et al.*, *The CLIC Physics Study Group*, http://cern.ch/CLICphysics.

[10] See TESLA Technical Design Report, Part IV, *A Detector for TESLA*.

[11] See TESLA Technical Design Report, Part II, *The Accelerator*.

[12] See TESLA Technical Design Report, Part VI, *Appendices*.

[13] See TESLA Technical Design Report, Part V, *The X-Ray Free Electron Laser*.

[14] F. Sauli, *GEM: A New Concept for Electron Amplification in Gas Detectors*, Nucl. Instrum. Meth. A386 (1997) 531.

[15] C. Quigg, Acta Phys. Polon. B30 (1999) 2145.

[16] The LEP Collaborations, ALEPH, DELPHI, L3, OPAL, the LEP Electroweak Working Group and the SLD Heavy Flavour and Electroweak Groups, LEPEWWG Note 2001/21, 2001.

[17] J. Alcaraz and E. Ruiz Morales, *Measuring the Top Yukawa Coupling to a Heavy Higgs Boson at future* e^+e^- *Linear Colliders*, Phys. Rev. Lett. 86 (2001) 3726.

[18] H.P. Nilles, Phys. Rep. 110 (1984) 1;
H.E. Haber and G.L. Kane, Phys. Rep. 117 (1985) 75.

[19] N. Arkani-Hamed, S. Dimopoulos and G. Dvali, Phys. Lett. B429 (1998) 263, Phys. Rev. D59 (1999) 086004;
I. Antoniadis, N. Arkani-Hamed, S. Dimopoulos and G. Dvali, Phys. Lett. B436 (1998) 257.

[20] T. Barklow, *LET Signals in* $e^+e^- \to WW$ *at* $\sqrt{s} = 800$ GeV, Proceedings of the 5th International Linear Collider Workshop (LCWS2000).

[21] S. Riemann, *Fermion-pair Production at a Linear Collider - A sensitive Tool for New Physics Searches*, Proceedings of the 5th International Linear Collider Workshop (LCWS2000), LC-TH-2001-007.

[22] P. Comas *et al.*, *The Physics of the* $e^+e^- \to t\bar{t}$ *Threshold Scan*, DESY 96-123 D.